Chapter 7
Sintering and Densification of Transparent Ceramics

7.1 Introduction

There are various sintering techniques that can be used to fabricate transparent ceramics. Conventional sintering techniques include vacuum sintering, hot pressing (HP), and hot isostatic pressing (HIP), while spark plasma sintering (SPS) is more popular than microwave sintering in the new sintering technique category. Every method has its own advantages and disadvantages. Different methods can be combined to offer higher sintering efficiency. The selection of sintering technique is also dependent on materials.

7.2 Vacuum Sintering

Vacuum sintering refers to a sintering process technique carried out with a vacuum equipment at a high vacuum level to achieve desired densification. Vacuum sintering has been widely used to fabricate various transparent ceramics, including garnet [1–7], spinel [8–11], alumina [12, 13], and rare earth sesquioxides ceramics, such as Y_2O_3 [14–18], Sc_2O_3 [19], pyrochlore oxides [20, 21], and so on.

When using vacuum sintering to fabricate YAG ceramics, the procedure usually consists of vacuum sintering followed by air annealing [22–38]. For example, transparent polycrystalline Nd:YAG ceramics can be synthesized by using solid-state reactive sintering the mixture of Al_2O_3, Y_2O_3, and Nd_2O_3 in a tungsten mesh-heated vacuum furnace (M60, Centorr Vacuum) at 5×10^{-6} Torr during holding [35]. Fully dense transparent samples with average grain sizes of $\sim$50 μm were obtained at 1800 °C. The sintering temperature was slightly affected by the concentration of Nd. A small amount of SiO_2 doping lowered the sintering temperature by $\sim$100 °C. SiO_2 is usually introduced by using tetraethyl orthosilicate (TEOS).

L.B. Kong et al., *Transparent Ceramics*, Topics in Mining,
Metallurgy and Materials Engineering, DOI 10.1007/978-3-319-18956-7_7

After sintering, the specimens were annealed at 1400 °C for 2 h in air for decoloring.

The first YAG transparent ceramics for laser applications was prepared by using vacuum sintering [5]. High-purity fine Al_2O_3 and Y_2O_3 powders presynthesized by using wet chemical methods, with the composition of YAG, were mixed with ethyl silicate as a solution of 0.5 wt% in ethyl alcohol, by using ball milling. After milling, the dried powder mixture was compacted by using isostatic pressing at 140 MPa. The pressed pellets were sintered at 1600–1850 °C at 1.3×10^{-3} Pa. Optical properties, microhardness, and thermal conductivity of the YAG ceramics sintered at 1800 °C were comparable with those of YAG single crystals.

Highly transparent polycrystalline Er^{3+}:$Y_3Al_5O_{12}$ (Er:YAG) ceramics with Er^{3+} ion concentrations of 1–90 % were prepared by using solid-state reaction combined with vacuum sintering technique [22]. Commercial powders of α-Al_2O_3, Y_2O_3, and Er_2O_3 with purity of >99.99 % were thoroughly mixed by using ball milling, according to Er:YAG compositions with different contents of Er, together with a trace of TEOS as sintering aid. The powder mixtures were dry-pressed at 3T to form pellets with a diameter of 25 mm, which were isostatically cold-pressed at 250 MPa. The pellets were vacuum sintered at temperatures of up to 1800 °C for different time durations at 10^{-3} Pa, after which they were annealed at 1450 °C for 20 h in air.

Figure 7.1 shows photographs of the mirror-polished Er:YAG transparent ceramics with different Er contents of from 1 to 90 %. With increasing content of Er, the specimens appeared pinker and pinker, due to the light absorption of Er^{3+} at the visible band. All the Er:YAG ceramics exhibited excellent optical properties.

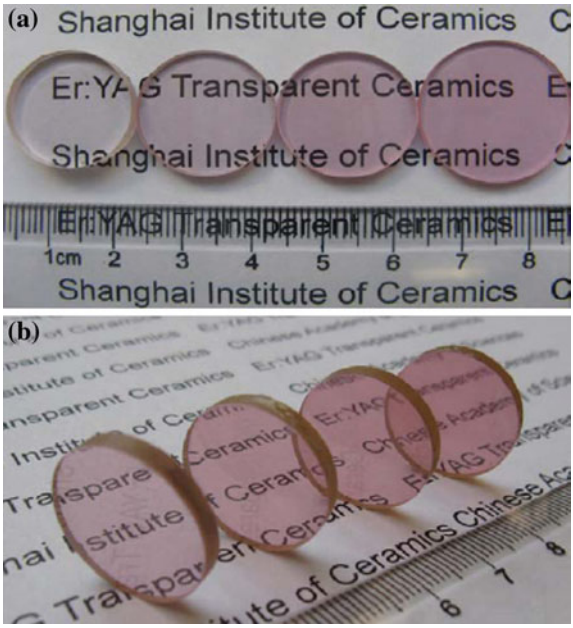

Fig. 7.1 Photographs of the mirror-polished Er:YAG ceramics with different contents of Er (from *left to right*): **a** 1, 5, 10, and 15 at.% and **b** 30, 50, 70, and 90 at.%. Reproduced with permission from [22]. Copyright © 2011, Elsevier

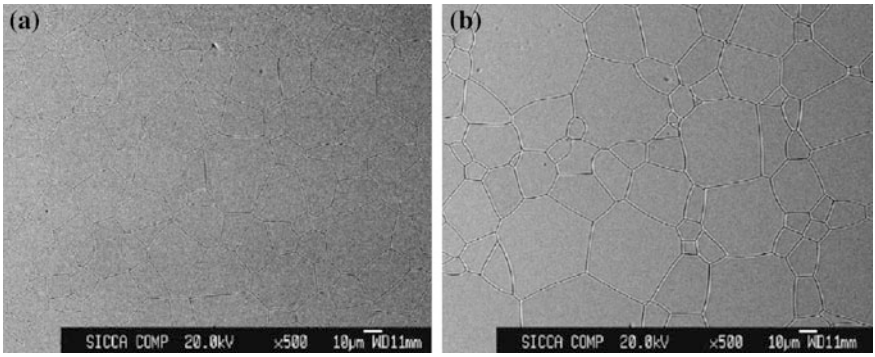

Fig. 7.2 Electron probe micro-analyzer (EPMA) images of the Er:YAG ceramics: **a** 1 % and **b** 90 %. Reproduced with permission from [22]. Copyright © 2011, Elsevier

EPMA images of the ceramics with 1 and 90 % Er are shown in Fig. 7.2. Both samples were very compact with very few pores. No secondary phases were observed both at the grain boundaries and in the inner grains. Average grain size of the 1 % Er:YAG ceramics was about 30 μm. The 90 % Er:YAG sample had a larger average grain size, probably due to the large particle size of starting Er_2O_3 powder. The high-resolution TEM (HRTEM) image indicated that the grain boundaries of the ceramics were clean and narrow, with a width of about 1 nm, thus leading to much negligible optical scattering.

It was found that there was a strong dependence of grain sizes on the location of the samples with green bodies formed by using uniaxial pressing with die, which actually indicated the presence of distributions in density of the green bodies. As mentioned before, cold isostatic pressing can only increase the density of the green body by <10 % and the density distribution of the green bodies would not be affected significantly. For two-directional pressing, the middle part of the green body possessed the lowest density, thus leading to largest grains after sintering. The grain size increased from the center part to the ends of the cylinder sample. For one-directional pressing, the density of the green body decreased from the top end to the bottom end. Figure 7.3 shows the scenario of one-directional pressing [22]. This observation is an agreement with previous discussion on ceramic powder packing.

Microstructural evolution during vacuum sintering of Nd:YAG transparent ceramics has been systematically studied [1]. Through microstructural observations, the microstructural maps and grain size density and grain size–pore size sintering trajectories of Nd:YAG ceramics, as a function of silica content, were established. For densities higher than 99.7 %, the occurrence of intragranular porosity was correlated to a critical pore radius of 0.16 μm. The presence of silica favored the formation of intragranular pores, which was attributed to the increase in the grain growth rate, as compared with the densification. An analytical model was established by coupling the analytical laws derived from sintering trajectories and the classical theory of light diffusion, which could be used to correlate the microstructural features of the transparent Nd:YAG ceramics to their optical properties.

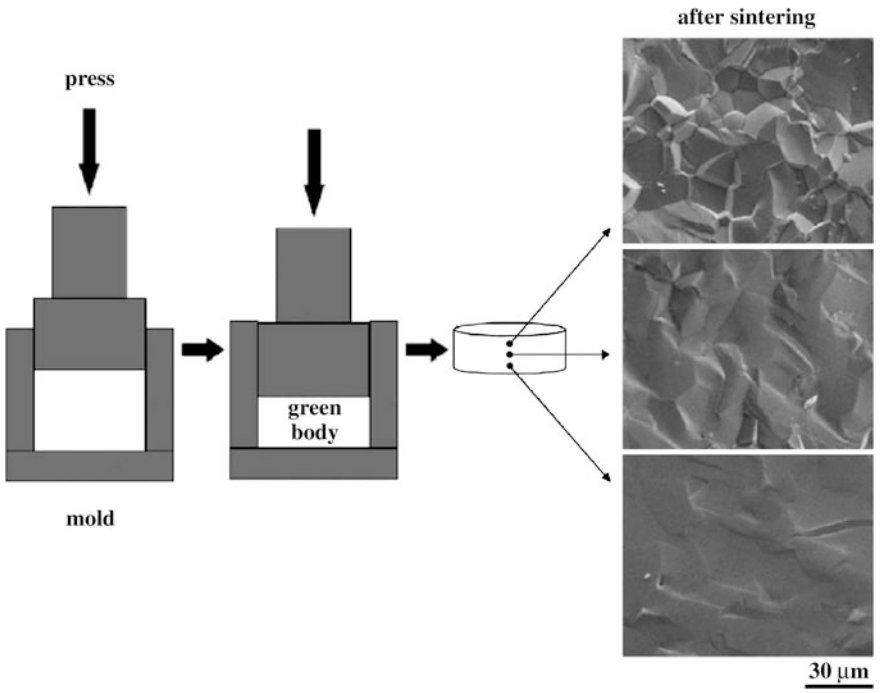

Fig. 7.3 Demonstration of the relationship between density and grain size distribution in a representative sample with green body formed by using one-directional axial press. Reproduced with permission from [22]. Copyright © 2011, Elsevier

Submicrometer α-Al_2O_3 (purity >99.99 %), Y_2O_3 (purity >99.99 %), and Nd_2O_3 (purity >99.99 %) powders were mixed to form the $Y_{2.94}Nd_{0.06}Al_5O_{12}$ (2 at.% Nd: YAG), by using ball milling in water with an organic dispersant and SiO_2 (purity >98 %) as sintering aid with contents of up to 0.3 wt%. Reactive sintering was conducted in a tungsten mesh-heated furnace at vacuum of $\leq 10^{-2}$ Pa and temperatures of 1000–1800 °C for different times durations, at heating/cooling rate of 5 °C min^{-1}.

Figure 7.4 shows SEM images of the undoped and 0.1 wt% SiO_2-doped Nd: YAG ceramics sintered at vacuum for 5 h at temperatures in the range of 1580–1730 °C [1]. Three types of microstructures could be observed, depending on the experimental parameters and the doping. Type one was porous microstructure, with the presence of open pores, having relative density (ρ) ranging from 60 to 90 % and submicrometer grain sizes of about 500 nm, as shown in Fig. 7.4a. Type two was dense microstructure, containing some closed intergranular pores, with relative density ranging from 90 to 99 % and micrometer grain sizes of about 1 μm, as illustrated in Fig. 7.4b. Type three was fully dense microstructure, with an average grain size of >1 μm, as seen in Fig. 7.4c–f. In the third-type microstructure, intragranular pores could occasionally be observed, as demonstrated in Fig. 7.4d. It

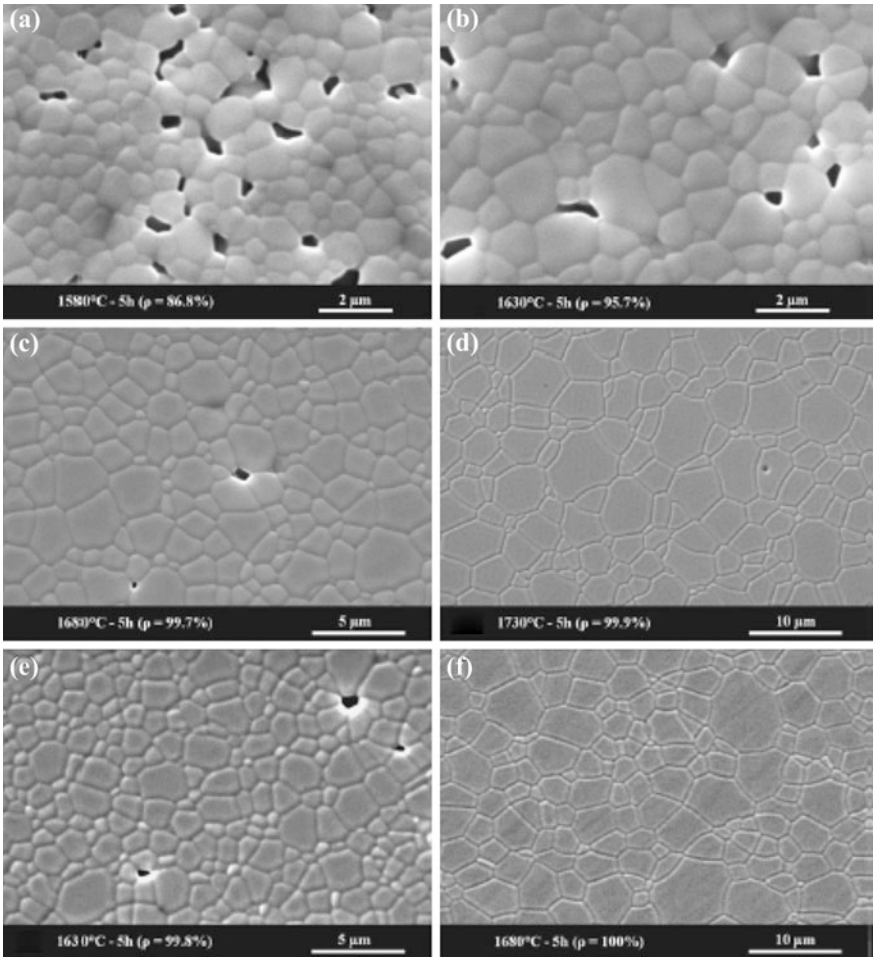

Fig. 7.4 SEM images of the undoped Nd:YAG ceramics sintered at vacuum for 5 h at temperatures of 1580 °C (**a**), 1630 °C (**b**), 1680 °C (**c**), and 1730 °C (**d**), as well as the 0.1 wt% SiO_2-doped Nd:YAG ceramics sintered for 5 h at 1630 °C (**e**) and 1680 °C (**f**). Reproduced with permission from [1]. Copyright © 2013, John Wiley & Sons

was shown that significant grain growth occurred at the final stage of the densification, i.e., with $\rho > 85$ %. The comparisons, between Fig. 7.4c–e, and d–f, indicated that the doping of 0.1 wt% of silica had no significant effect on overall microstructural profiles of the Nd:YAG ceramics, but could decrease the sintering temperature by about 50 °C correspondingly.

Sintering trajectories, i.e., grain size (G) versus relative density (ρ), of the undoped and silica-doped samples sintered for 2 h at 1450–1800 °C, are shown in Fig. 7.5 [11]. It was observed that grain size increased at a very slow rate until the

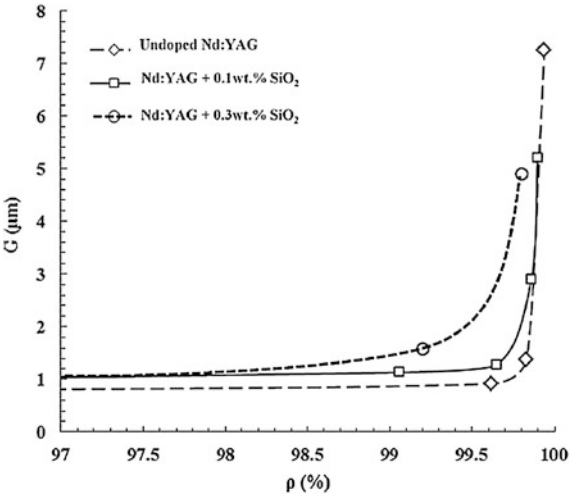

Fig. 7.5 *G–ρ* sintering trajectories of the undoped and silica-doped Nd:YAG ceramics sintered at vacuum for 2 h at temperatures ranging from 1450 to 1800 °C. Reproduced with permission from [1]. Copyright © 2013, John Wiley & Sons

relative density approached 99 %. However, after that, there was a sharp increase in grain size. The presence of silica could promote grain growth and densification.

Transmittance spectra of the samples with a thickness of 2.5 mm, labeled with their corresponding pore volume densities, are shown in Fig. 7.6a [11]. Obviously, the baseline of transmittance increased with decreasing volume density of the pores, demonstrating the optical scattering effect of pores in the Nd:YAG ceramics. Photographs of the corresponding Nd:YAG ceramic samples are shown in Fig. 7.6b. Analytical model indicated that the attenuation coefficient could be linked to the volume density of pores. It was concluded that once having similar values in pore volume density, e.g., $<3 \times 10^3$ cm^3, Nd:YAG ceramics could have similar optical properties of their single-crystal counterparts. This study provided a useful reference to other transparent ceramic materials.

Transparent alumina ceramics with high transmission have been developed by using a rapid vacuum sintering processing at a lower sintering temperature and shorter time duration, as compared with the conventional pressureless sintering [13]. The alumina sintered at 1670 °C for 5 min exhibited a residual porosity of as low as 0.002 %, thus showing a real in-line transmission of 64 % at of 1100 nm. The sintering time had an effect on the densification and transparency of the alumina ceramics sintered at 1650 °C.

A high-purity commercial α-Al_2O_3 (99.99 %) was mixed with 0.1 wt% MgO (99.99 %, 30 nm) as sintering aid by using ball milling with high-purity alumina balls. The milled and dried mixture was made into pellets with diameter of 15 mm and thickness of 2 mm at a uniaxial pressure of 200 MPa. The green pellets were presintered at 1200 °C for 2 h in muffle furnace and finally sintered in vacuum at 1500–1700 °C for 0–30 min, at a heating rate of 100 °C min^{-1}, which was followed by a natural cooling. All sintered samples were mirror-polished on both surfaces and thermally etched at 1400 °C for 1 h in air.

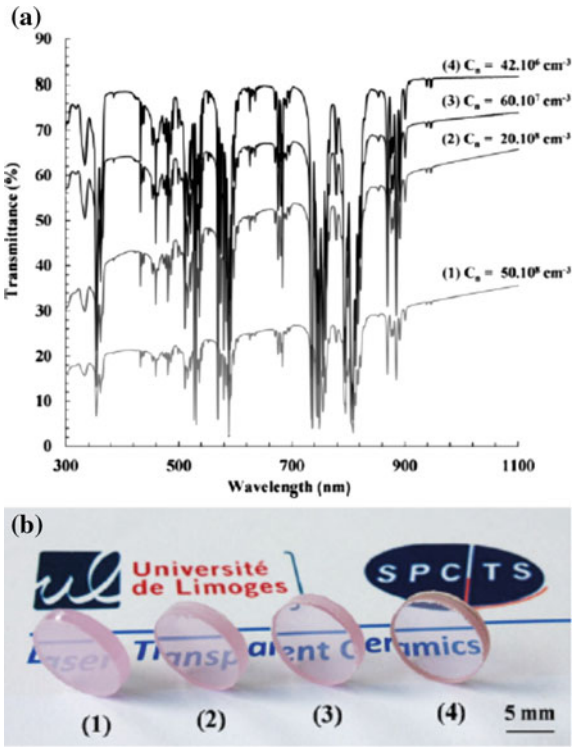

Fig. 7.6 **a** Optical transmittance spectra of the 0.3 wt% SiO_2-doped Nd:YAG transparent ceramics with different pore volume densities (C_n) after sintering at vacuum (samples thickness was 2.5 mm). **b** Photographs of the Nd:YAG ceramics corresponding to the samples in (**a**). Reproduced with permission from [1]. Copyright © 2013, John Wiley & Sons

SEM images of the ceramics sintered at different temperatures are shown in Fig. 7.7 [13]. Porosities of the samples sintered at 1570, 1600, 1650, and 1670 °C for 5 min were 1.256, 0.705, 0.075, and 0.002 %, with corresponding average grain sizes of 3.54, 5.47, 8.55, and 11.14 μm, respectively. Both the grain size and density of the samples were increased with increasing sintering temperature. A total of 1600 °C was the critical temperature for complete densification, above which all the samples demonstrated a homogeneous microstructure with clear grain boundaries and without abnormal grain growth.

Figure 7.8 shows SEM images of the samples sintered at 1650 °C for different time durations [13]. All samples exhibited very high density, homogeneous microstructure, and clear grain boundary, although residual pores at triple junction points of grain boundary were occasionally observed. It was found that prolonged sintering time resulted in an increase in pore size.

During the rapid vacuum sintering, the densification process of the transparent alumina can be attributed to the presence of a temperature gradient in the sample and the formation of nonequilibrium grain boundaries [39, 40]. The nonequilibrium grain boundaries had higher energy, thus providing a stronger driving force for grain growth. At the same time, due to the large thickness of the nonequilibrium grain boundaries, the grain-boundary mobility was decreased. Therefore, densification was maintained, while grain growth was suppressed.

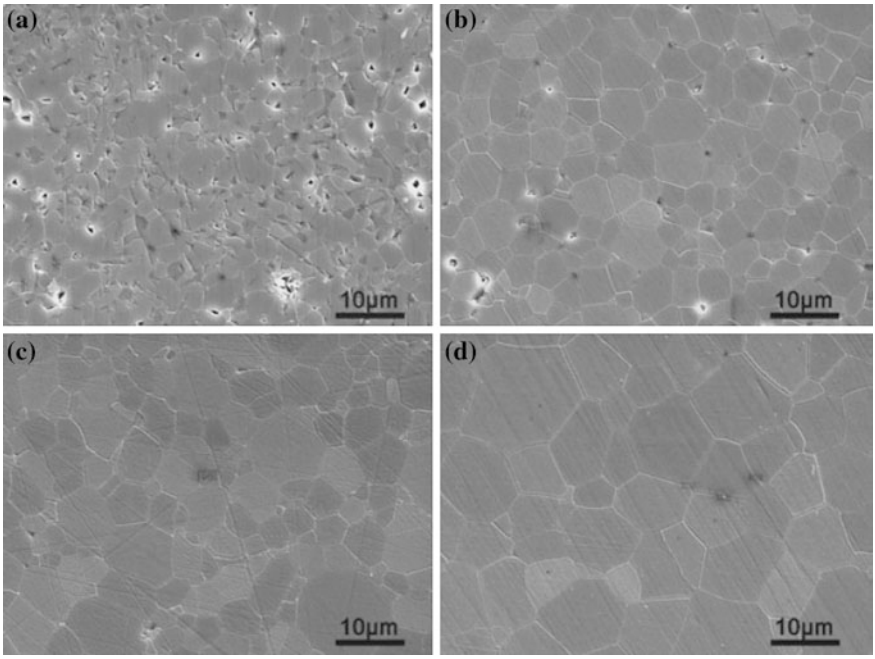

Fig. 7.7 SEM images of the alumina ceramics sintered for 5 min at different temperatures: **a** 1570 °C, **b** 1600 °C, **c** 1650 °C, and **d** 1670 °C. Reproduced with permission from [13]. Copyright © 2012, John Wiley & Sons

The mechanism for the improvement in transparency of vacuum sintered Y_2O_3 ceramics due to the addition of ZrO_2 has been analyzed [41]. Y_2O_3 (99.999 %) and ZrO_2 (99.99 %,) with an average particle size of 1 μm were mixed, according to the formula of $(Y_{1-x}Zr_x)_2O_3$ (x = 0–0.10), by using a ball milled in absolute ethyl alcohol with agate balls. After milling and drying, pellets with 20 mm in diameter were formed with stainless steel at 15 MPa and then isostatically pressed at 250 MPa. Sintering was conducted at 1800 °C for 15 h in vacuum.

Combined with sintering kinetics, thermodynamics, and experimental results, the mechanism of ZrO_2 in improving the transparency of Y_2O_3 ceramic was clarified. The addition of ZrO_2 led to the formation of ZrO_2–Y_2O_3 binary system with decreased melting point, thus reducing the sintering temperature. The radius of Zr^{4+} is 0.80 Å, which is close to that of Y^{3+} (0.90 Å), so that there was only very small lattice distortion when Y^{3+} was substituted with Zr^{4+}.

At the final stage of sintering, grains with large size and low surface energy tend to grow at the expense of the surrounding smaller grains, which is known as discontinuous or exaggerated grain growth. During this process, due to the high mobility of grain boundaries, pores are easily trapped in grains, which is harmful to

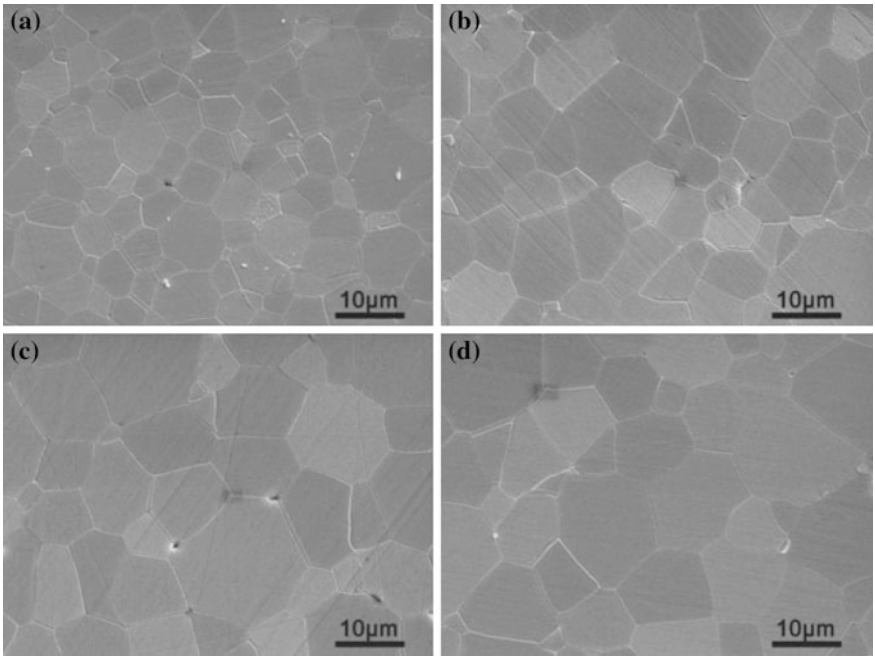

Fig. 7.8 SEM images of the alumina ceramics sintered at 1650 °C for different time durations: **a** 0 min, **b** 10 min, **c** 20 min, and **d** 30 min. Reproduced with permission from [13]. Copyright © 2012, John Wiley & Sons

the transparency. Due to its high melting point (2715 °C), ZrO_2 is prone to form solid solution at the grain boundaries, so as to reduce the grain-boundary mobility. At the same time, secondary recrystallization could occur, due to the solute drag mechanism, which would be beneficial to the elimination of pores and the homogenization of grain sizes, two critical factors to ensure high optical transmittance of the Y_2O_3 ceramics.

It is well known that the diffusion coefficient of O^{2-} is much higher than that of Y^{3+} in pure Y_2O_3. Therefore, cation diffusion is the rate-controlling step of grain-boundary migration, i.e., the diffusion of $[Y_i^{\cdots}]$ dominates the grain-boundary mobility [42]. There are following defects and defect reactions in Y_2O_3.

For Schottky defects, there is:

$$Y_2O_3 \Leftrightarrow 2V_Y''' + 3V_O^{\cdot\cdot}. \tag{7.1}$$

For Frenkel defects, there are:

$$O_O \Leftrightarrow O_i'' + V_O^{\cdot\cdot}, \tag{7.2}$$

$$YY \Leftrightarrow V_Y''' + Y_i^{\cdots}. \tag{7.3}$$

After doping with ZrO_2, there is:

$$2ZrO_2 \longrightarrow Y_2O_3 2Zr_Y^{\cdot} + O_i'' + 3O_O. \tag{7.4}$$

As a result, when every two Zr^{4+} ions were substituted, one O_i'' was produced, so that $[V_Y''']$ was increased, while $[Y_i^{\cdots}]$ was decreased. The decrease in $[Y_i^{\cdots}]$ resulted in a reduction in grain-boundary mobility and sintering rate, which ensured the escape of pores and densification of the ceramics. For example, average grain size of the ZrO_2-doped ceramics was about 15 μm, which was much smaller than those widely reported in the open literature. In terms of optical performance of the transparent ceramics, 3 at.% ZrO_2 was the optimized doping concentration.

7.3 Hot Pressure (HP) Sintering

Hot pressure (HP) sintering is a high-pressure low-strain-rate powder metallurgy process, which is used to form a powder or powder compact at a temperature that is sufficiently high to induce sintering and creep processes. This is achieved by the simultaneous application of heat and pressure. Densification at high pressure proceeds through the rearrangement of particles and plastic flow at the particle contacts. HP is mainly used to fabricate hard and brittle materials. As a result, HP has become an important technique to obtain transparent ceramics.

In 1977, transparent spinel with small grain size (1–2 μm) was prepared by using low-temperature (1400 °C) and high-pressure (70 MPa) hot pressing [43]. Transparent magnesia–alumina spinel ceramics were prepared from equimolar mixture of the oxides, which were derived from $Mg(OH)_2$ and $Al(OH)_3$ after calcining at 900 °C for 2 h and 1400 °C for 2 h, respectively. Formation of spinel from the oxide mixture was accompanied with a volume expansion of about 7.9 %, which was suppressed by applying a pressure of >330 kg cm^{-2} at 950 °C, so as to promote the densification of the spinel ceramics. A step heating schedule was used, i.e., hot-pressing technique at 770 kg cm^{-2} at 1300 and 1350 °C for 0.5 h and 1400 °C for 1 h. The transparent spinel ceramics exhibited optical transmittance of 35–75 % in the visible range and 75–85 % in the IR range.

Since then, HP became a widely used technique to prepare transparent spinel ceramics. For example, HP process was used to fabricate $MgAl_2O_4$ transparent ceramics, with a nearly 100 % densification [44]. Spinel powders for the production of transparent polycrystalline ceramic windows were produced by using both the traditional ceramic solid-state reaction and solgel methods. Among them, the powders produced from the reaction of organomagnesium compounds with surface modified boehmite precursors were best to produce high-quality transparent spinel ceramics. The powder synthesis method allowed fine control over the particle size,

size distribution, purity, and stoichiometry. The process involved the formation of a boehmite solgel from the hydrolysis of aluminum alkoxides. The boehmite nanoparticles were treated through a surface modification with carboxylic acids. The surface modified boehmite nanoparticles were then used to make a precursor powder of pure phase spinel through metal exchange at room temperature with magnesium acetylacetonate.

Different from the conventional sintering process which usually requires high sintering temperatures (>1600 °C), HP process is able to achieve desired densification at relatively low temperature, which is therefore also called low-temperature high-pressure (LTHP) process. Due to its low-temperature requirement, it can be used to develop nanosized ceramics [45–48]. The sintering mechanism at high pressures is entirely different from that at ambient pressure [45]. High pressure can suppress the grain growth and initiate plastic deformation to eliminate pores and/or additional phases existing in triple junctions of the grains. However, the conventional sintering process is controlled by grain growth to avoid imperfections between grain boundaries when preparing transparent ceramics.

High-resolution transmission electron microscopy (HRTEM) and selected area electron diffraction (SAED) of two selected samples, sintered at 4.0 GPa at 600 °C and 4.0 GPa at 1100 °C, are shown in Fig. 7.9 [45]. The average grain size observed from Fig. 7.9a was about 40 nm. The nanostructured profile of the sample was confirmed by the corresponding SAED pattern. The HRTEM image showed a clear grain boundary without any secondary phase and/or in-between phases, as demonstrated in Fig. 7.9b. The clean grain boundaries had no contribution to scattering, which was responsible for the high transparency of the $MgAl_2O_4$ ceramics sintered at 4.0 GPa at 600 °C.

As the sintering temperature was increased to 1100 °C, the grain/crystallite size increased significantly, so that the nanostructured profile was lost due to the grain growth, as illustrated in Fig. 7.9c. It is also found that the crystals have a wider particle size distribution, probably due to the presence of a temperature gradient in the sample. Consequently, imperfections, nonuniform crystallites and irregular grain boundaries, were present, which would pose negative effects on optical transparency of the ceramics. The HRTEM image of $MgAl_2O_4$ ceramics sintered at 4.0 GPa at 1100 °C taken along the [332] zone axis, shown in Fig. 7.9d, together with the corresponding SAED pattern, indicated a highly crystallized feature of the sample, demonstrating the grain growth of the materials at 1100 °C.

Therefore, the formation temperature of the transparent $MgAl_2O_4$ spinel ceramics could be significantly reduced, if sufficiently high pressure is available. As the pressure is in the range of 2–5 GPa, very low sintering temperatures of 500–700 °C can lead to nanosized transparent spinel ceramics [46]. The nanosized ceramics were highly transparent even though their relative densities are less than 99 %, due to the low or negligible light scattering from the nanosized grains and pores. The LTHP process is able to densify nanosized powders without significant grain growth, which becomes a key advantage for the development of transparent ceramics, as discussed above. It is of special interest when mechanical strength is an important requirement.

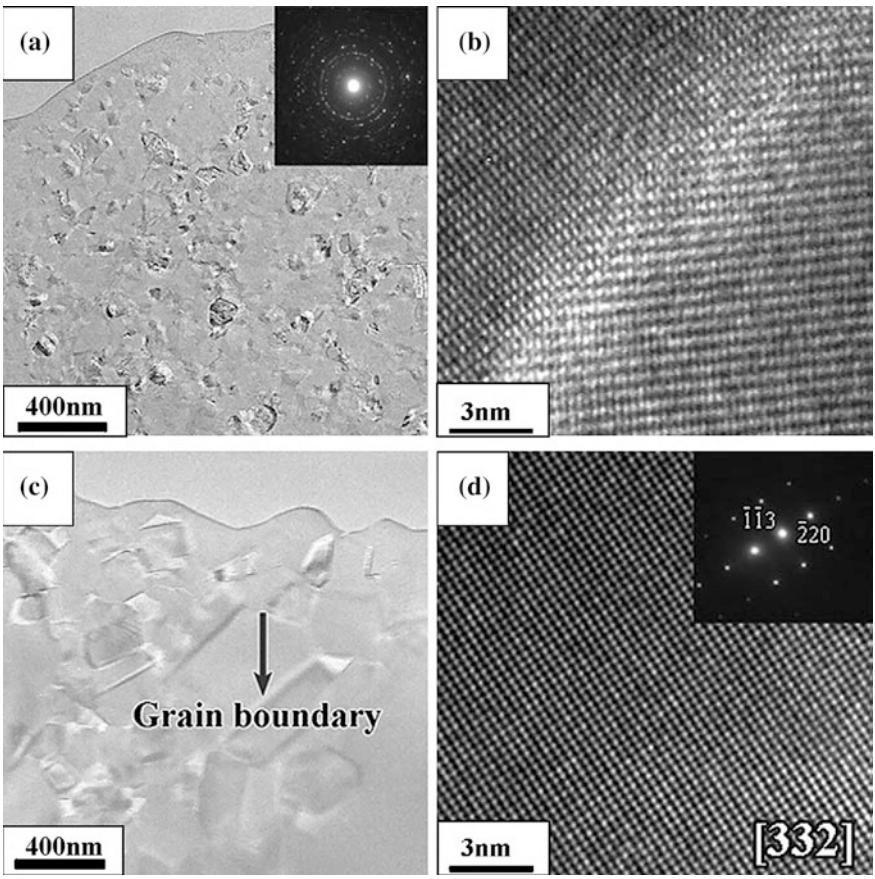

Fig. 7.9 **a** TEM image showing microstructure of the $MgAl_2O_4$ nanocrystalline transparent ceramics sintered at 4.0 GPa and 600 °C for 30 min. The corresponding SAED pattern in the inset proved the characteristics of the polycrystalline nanograins. **b** HRTEM image of the $MgAl_2O_4$ nanoceramics. **c** TEM image showing microstructure of the $MgAl_2O_4$ ceramics sintered at 4.0 GPa at 1100 °C for 30 min, with an average grain size of the smaller crystallites to be ~500 nm. **d** HRTEM image of the $MgAl_2O_4$ ceramics sintered at 4.0 GPa/1100 °C taken along the [332] direction, with the corresponding SAED pattern shown as the inset. Reproduced with permission from [45]. Copyright © 2010, Elsevier

Another example is the development of a nanocrystalline spinel ceramics with 50 % increase in hardness by using hot pressing [49]. It is well accepted that mechanical strength and hardness of a material can be increased by decreasing its grain size, as described by the empirical Hall–Petch relationship [50, 51]. Based on this principle, an integrated approach was developed by using nanosized spinel powder, combined with high-pressure and low-temperature sintering to fabricate fully dense and high-purity nanocrystalline ceramics with nanometer-sized grains. The Hall–Petch relationship was confirmed by the hardness of the transparent spinel ceramics with grain sizes down 28 nm. As a result, the nanosized spinel ceramics

exhibited a 50 % increase in hardness without a decline in fracture resistance. More importantly, the nanocrystalline spinel ceramics had near theoretical optical transparency.

Figure 7.10 shows a schematic diagram of the high-pressure high-temperature sample holder [49]. Spinel powders were pressed into green compacts without binder within glove box in an evacuable die at 1900 kg cm^{-2}. The ejected green compacts were mechanically sealed in a metal capsule. The sealed sample capsule was inserted into the high-pressure assembly, which consisted of a partially sintered ZrO_2 container saturated with CsCl in the shape of a rectangular cuboid with truncated edges, a graphite heater, mica, and molybdenum heater contacts. K-type thermocouples were inserted through both high-pressure cell assembly lids. A pressed boron nitride tablet isolated the exposed thermocouple junction from the metal sample capsule. High-pressure experiments were performed in a pressless split-sphere apparatus (BARS) equipped with an 8–6-type multi-anvil system. After about 25 min pressurization to 2 GPa, samples were sintered at temperatures from 740 to 845 °C for 15 min. The nanosized spinel ceramics are transparent in the visible spectrum, without major absorption bands from ultraviolet to short-infrared wavelengths. The maximum transmission was about 81 % at infrared wavelengths of 1200–1350 nm.

The fact that the ceramics were fully dense and of high quality, without residual porosity or obvious grain growth, was further confirmed by the SEM and TEM images, as shown in Figs. 7.11 and 7.12 [49]. SEM images of the polished surface of the ceramics derived from the 200 nm powder and the same 30.8 nm nanocrystalline ceramics are shown in Fig. 7.11a, b, respectively. Any potential variability in the sintering environment has been eliminated, because the samples were sintered in the same sample capsule at 2 GPa and 795 °C. Fine pores were present in the submicron sample, while very few features, which included a surface scratch and dust particles, were present at similar magnification for the nanocrystalline

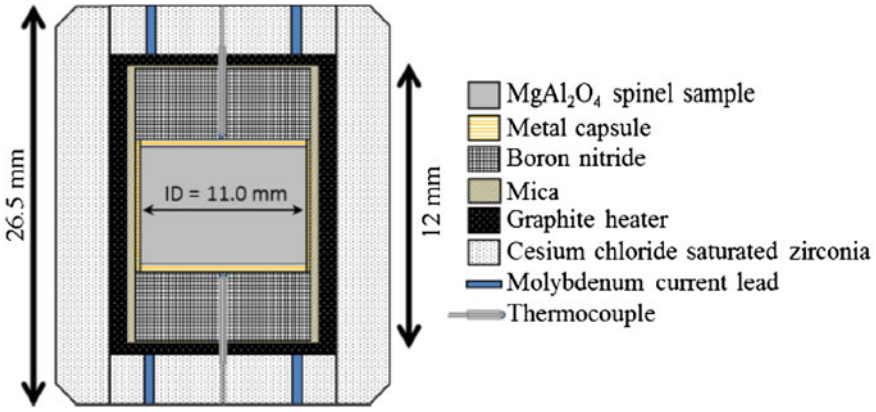

Fig. 7.10 Schematic of the high-pressure cell assembly. Reproduced with permission from [49]. Copyright © 2014, Elsevier

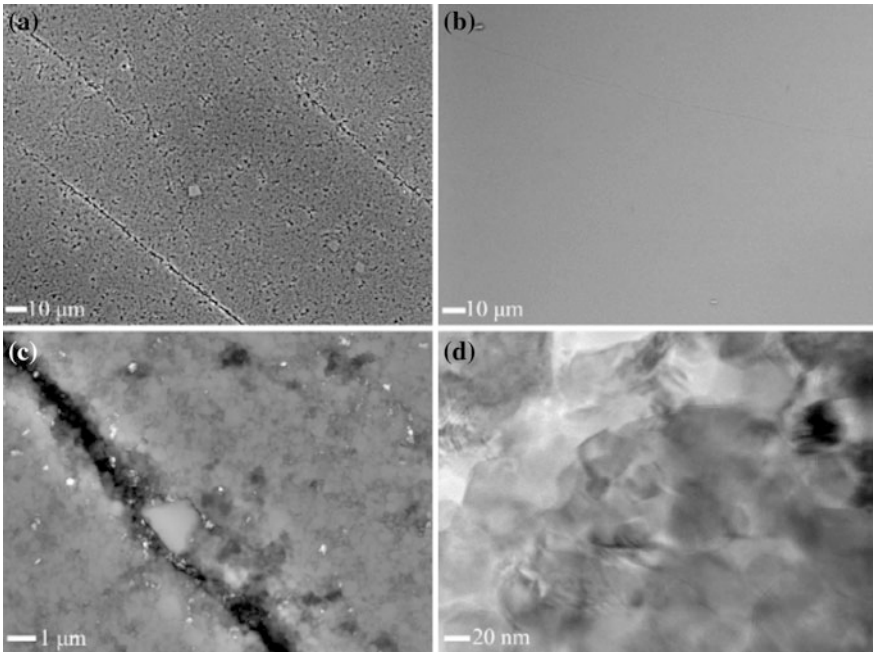

Fig. 7.11 Microstructures of the porous and fully dense spinel ceramics produced by sintering at 2 GPa and 795 °C. **a** and **c** SEM micrographs of the porous submicron structure of spinel ceramic derived from 200-nm-sized spinel powder. **b** SEM and **d** TEM images of the microstructure of the fully dense nanosized spinel ceramics. Reproduced with permission from [49]. Copyright © 2014, Elsevier

ceramics. At higher magnifications, a submicron grain structure was observed in the coarse ceramics and abnormally large grains were present along with the porous structure. The grain structures of the nanocrystalline ceramics are clearly demonstrated by the TEM images, as shown in Figs. 7.11d and 7.12.

Figure 7.12 shows TEM images of different grain-boundary regions of the nanosized spinel ceramics [49]. There were nanoscale grains where the crystalline lattice extended into the boundary, as shown in Fig. 7.12a, d. Also, grain boundaries decorated with a small, ~ 1 nm, amorphous phase region were observed, as shown in Fig. 7.12b. Such amorphous phases were also present at the junctions of three grains, as shown in Fig. 7.11c. Noticing the highly transparent characteristics of the nanosized sample, the slight fraction of amorphous phase at the grain boundaries had negligible influence on its optical properties and density.

Similar process was also used to develop yttrium aluminum garnet ($Y_3Al_5O_{12}$, YAG) transparent ceramics with nanosized grains [52]. In this study, a high-pressure cell was used, where disk samples were placed in a capsule made of NaCl, both to ensure the quasi-hydrostatic compression of the sample and prevent its contact with the graphite heater. The whole structure was then contained in the pyrophyllite high-pressure cell. The sample temperature in the high-pressure cell

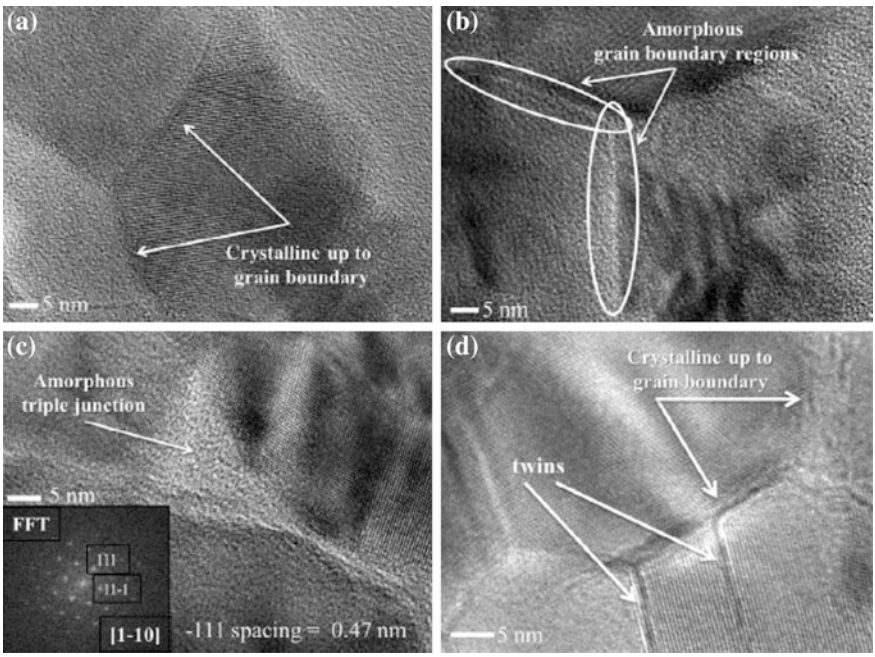

Fig. 7.12 TEM images of the fully dense nanosized spinel ceramics produced by sintering at 2 GPa and 795 °C. **a** and **b** Different areas revealing that some grain boundaries contain ~1-nm amorphous phase regions. **c** An amorphous triple junction with the inset showing the fast Fourier transform of the main figure. **d** Image from a region containing nanotwins. Reproduced with permission from [49]. Copyright © 2014, Elsevier

was measured directly by using a standard Ni–Cr/Ni–Si thermocouple. The cell pressure was monitored by using a calibrated oil pressure meter. Desired pressures were first applied to the samples before raising the temperature. The pressure range was 2.0–5.0 GPa, and temperature range was 300–500 °C, with holding time of 30 min. After that, the pressure was released first, and then, the samples were cooled down to room temperature at a rate of 15 °C min^{-1}. By doing in this way, the residual stress of the samples could be released in order to avoid the happening of cracking. Optimized processing parameters for transparent YAG ceramics were 5 GPa and 450 °C.

One of the characteristics of HP is freedom to optimize the sintering parameters, which has been demonstrated when HP sintering was used to fabricate transparent Y_2O_3 ceramics [53, 54]. For instance, stepwise process has been reported to fabricate Eu:Y_2O_3 transparent ceramics [54]. The program included a high-temperature ramp at constant pressure and a pressure ramp at constant high temperature. After a dwell at 1150 °C to outgas the samples, a pressure of 10 MPa was applied, followed by a temperature ramp to 1580 °C at a heating rate of 8 °C min^{-1}. After a 30 min dwell at constant temperature and pressure, the pressure was raised to 40 MPa at a

rate of 0.4 MPa min^{-1}. With this stepwise application of pressure, optimized temperature was 1580 °C.

HP sintering process is a very unique and feasible technique to prepare transparent electro-optic ceramics, including PLZT [55–57], PZN–PLZT [58] and PMN–PT [56, 59–61], and other ferroelectric ceramics [62], which contain volatile element Pb. In the early 1970s, (Pb, La)(Zr, Ti)O_3 (PLZT) transparent ferroelectric ceramics were synthesized by using HP [43]. The transparent PLZT ferroelectric ceramic materials have found a variety of electrooptic applications. They were prepared from mixed oxides by using hot-pressing sintering at 1100 °C for 16 h at 2000 psi. Transmission measurements in the visible and infrared showed that these materials exhibited a nearly constant response from the absorption edge of 0.37 μm to ~6 μm. The highest transmission values were observed for compositions containing >8 at.% La. Specific compositions exhibited electro-optic memory, conventional linear, and quadratic electrooptic effects, with performances comparable with those of single crystals.

Highly transparent ceramics of La-doped 0.75Pb($Mg_{1/3}Nb_{2/3}$)O_3–0.25$PbTiO_3$ (PMN–PT) were fabricated by using a two-stage sintering method [59]. Green pellets were first sintered in an oxygen atmosphere (OA) at different temperatures, which were then hot pressed (HP) at temperatures of >1000 °C for more than 8 h at pressures of 50–100 MPa. The ceramics prepared in this way exhibited a transparency of as high as 65 % at infrared wavelength. Large quadratic electro-optic coefficient of 66×10^{-16} $(m/v)^2$ was obtained, which was the highest value reported in the literature for the ceramics with similar compositions.

The precursor powder with a composition of La-doped PMN–PT 3/75/25 was synthesized by using the columbite precursor method, starting with PbO, MgO, Nb_2O_5, TiO_2, and La_2O_3, in which small amount of excessive PbO was used to promote the densification through liquid-phase sintering. The powder was made into pellets by using uniaxial pressing. The pellets were first sintered in an OA at different temperatures. The sintered pellets were then hot pressed (HP) at a temperature of >1000 °C for more than 8 h at pressures of 50–100 MPa. In the OA–HP two-stage sintering method, the OA sintering temperatures were different: (A) 1150 °C, OA–HP; (B) 1200 °C, OA–HP; and (C) 1230 °C, OA–HP.

The PMN–PT ceramics exhibited a transparency of as high as 65 % in infrared region, as shown in Fig. 7.13a. SEM images of PMN–PT 3/75/25 ceramics sintered with different schedules are shown in Fig. 7.13b, c. All samples showed transgranular fracture character, which was attributed to the increased homogeneity between grain boundary and grain, as well as firm conjunct strength of grains caused by the liquid phase that was formed during the sintering. It was found that the sample with more transgranular fracture had higher transparency, which suggested that grain boundary with an increased homogeneity and firm strength would have reduced reflection and scattering of light. This observation once again indicates that the quality of grain boundary plays a more important role in determining optical properties of transparent ceramics, as discussed previously.

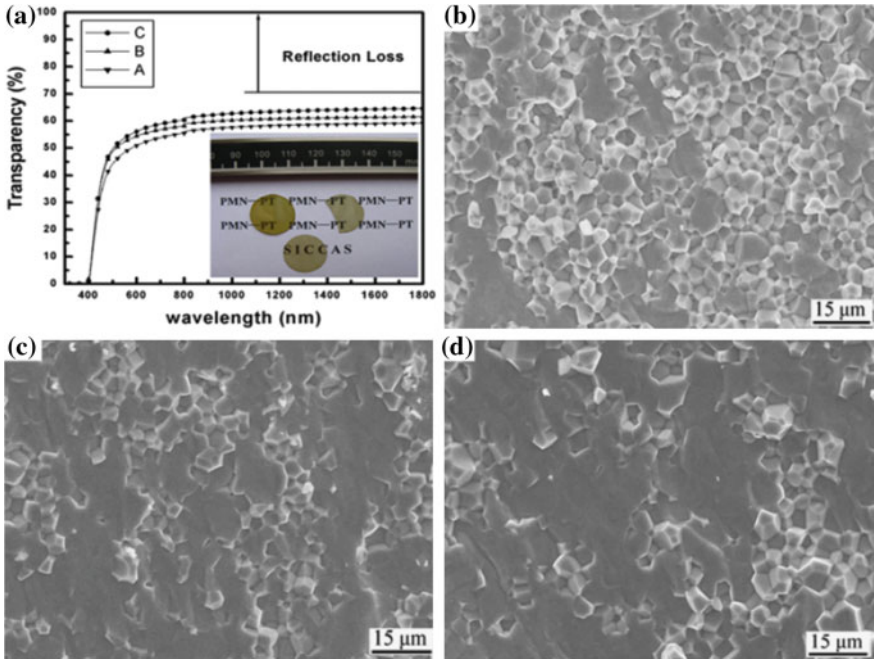

Fig. 7.13 Transmission curves of the PMN–PT 3/75/25 ceramics with a thickness of 0.5 mm (**a**) and SEM images of the samples sintered with different schedules: **b** sample A, **c** sample B, and **d** sample C. Reproduced with permission from [59]. Copyright © 2010, John Wiley & Sons

HP process was found to be the most feasible method to prepare transparent or translucent α-sialon ceramics [63, 64], which could not be achieved by using the conventional pressless sintering. Single-phase α-sialon ceramics with high optical transmittance have been prepared by using hot pressing [63]. HP was also used to tailor grain morphologies and preferential texturing microstructures of α-sialon ceramics [64–66]. Other examples include translucent MgO ceramics fabricated by using hot-pressing, with nanopowder of MgO containing 2–4 % LiF as a sintering aid [67]. HP process has even been used to prepare fluoride ceramics (CaF_2), such as transparent Yb:CaF_2 ceramics [68, 69].

7.4 Hot Isostatic Pressure (HIP) Sintering

Hot isostatic pressing (HIP) is a fabrication process that is used to reduce the porosity of metals and increase the density of various ceramic materials [70–74]. The HIP process subjects a component to both elevated temperature and isostatic gas pressure in a high-pressure containment vessel. The chamber is heated, causing the pressure inside the vessel to increase. Many systems use associated gas

pumping to achieve the desired pressure levels. Pressure is applied to the material from all directions.

Materials are hot isostatically pressed (HIPed) in order to achieve the maximum possible densification, which has become a key technique to achieve high optical transmittance. To reduce the fabrication cost, hot isostatic pressing is usually used as the last step, although it has been proved to be a critical step to prepare high-quality transparent ceramics. This is simply because HIP involves sophisticates equipment and critical experimental conditions.

HIP process has been widely used to synthesize transparent armor ceramics, such as alumina (Al_2O_3) [75–79], YAG [80–83], and spinel ($MgAl_2O_4$) [84–88]. HIP process can be combined with HP. Hot pressing followed by hot isostatic pressing (HIP) proved to be more feasible to fabricate transparent $MgAl_2O_4$ ceramics was widely used [84, 85, 88]. Nowadays, HIP process is also used to synthesize cubic sesquioxide ceramics, including Y_2O_3 [89], Sc_2O_3 [90], and Lu_2O_3 [91]. In these cases, vacuum sintering to remove closed pores with a subsequent HIP step was usually employed, which provided an alternate processing route to the fabrication of fully dense sesquioxide ceramics with less possibility for contamination and reduction than hot pressing.

A simple method has been established to achieve nearly 100 % relative density of α–alumina ceramics by using hot isostatic pressing (HIP) [75]. In this study, transparencies of the samples were correlated to their grain size and residual porosity. A commercially available α-alumina powder was wet milled in order to realize de-agglomeration. After that, the average particle size of the powder was 100–150 nm. Suspensions with ~75 wt% solid with any organic additive were cast with a nylon filter (pore diameter = 0.2 μm) to form green bodies. The wet bodies were dried at 65 °C for 15 h and then calcined at 600 °C for 30 min in vacuum of <1 mbar. Then, the samples were sintered naturally in vacuum of $\sim 10^{-6}$ mbar at temperatures of about 1200 °C for 2–17 h. The samples with porosities of <10 % were subject to HIP at about 1200 °C at 170 MPa in argon for 3–5 h. The HIP furnace was made of molybdenum. The densities of the HIP processed samples were measured with a very precise method, by measuring mass of the ceramics outside and inside water, which were then compared with the density of alumina single crystal to obtain relative densities.

Figure 7.14 shows porosity values of the samples after natural sintering in vacuum versus the treatment temperature and time [75]. With a constant treatment time, the porosity always increases as the sintering temperature is decreased. It was found in this work that if the porosity was higher than 8 %, the HIP treatment was not workable. The samples sintered at 1200 and 1220 °C; time duration of 2 h was sufficient. However, the samples sintered at 1170 and 1185 °C should be kept for 17 h to decrease the porosity to be <4 %.

In addition, the treatment temperature and time also showed their effects on grain size of the samples, as shown in Fig. 7.15 [75]. As stated earlier, the grain size of the starting powder was 100–150 nm. After the treatments at 1200 and 1220 °C for 2 h, the grain size was <400 nm, which was close to that of the sample sintered at 1170 °C for 17 h. However, after sintering at 1185 °C for 17 h, the grain size was

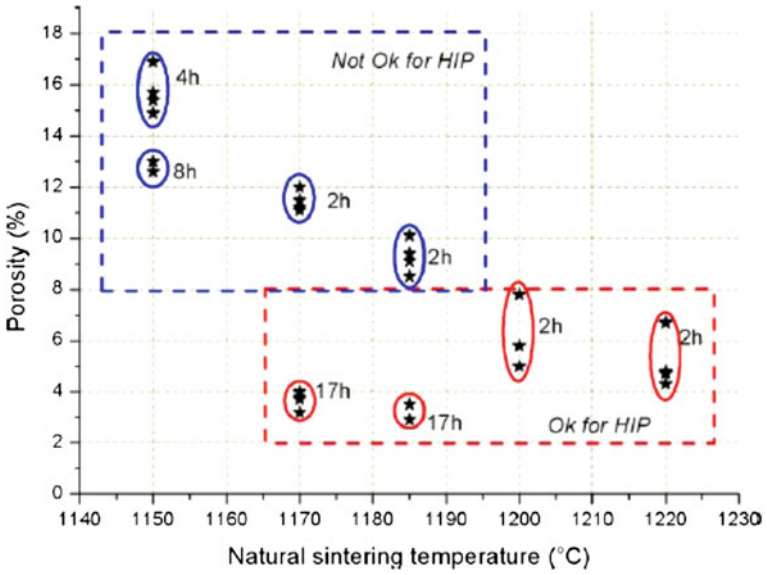

Fig. 7.14 Total porosity versus the natural sintering temperature, for different treatment times, at the pressure of ~10^{-6} mbar. Reproduced with permission from [75]. Copyright © 2011, Elsevier

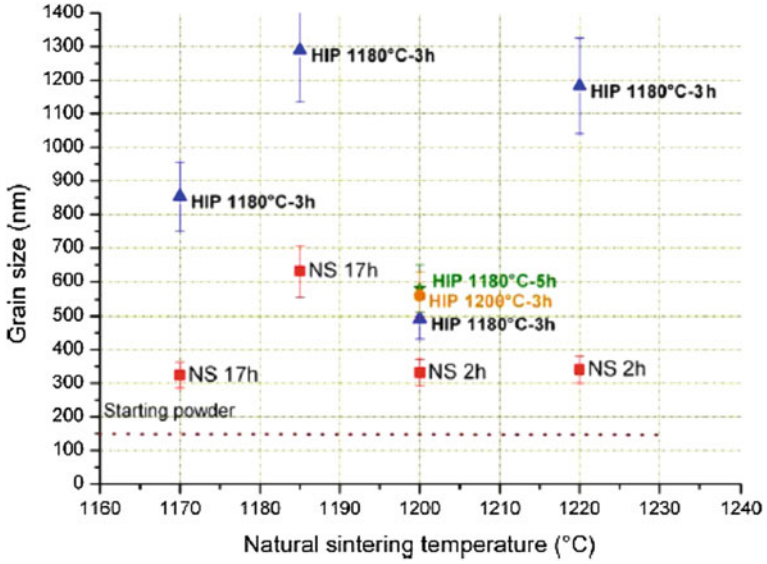

Fig. 7.15 Grain sizes of the ceramics versus the natural sintering (NS) temperature: (*square*) after natural sintering, (*triangle*) after HIP at 1180 °C and 170 MPa for 3 h, (*disc*) after HIP at 1200 °C and 170 MPa for 3 h, and (*star*) after HIP at 1180 °C and 170 MPa for 5 h. The HIPed ceramic values are placed versus the temperature of the corresponding natural sintering. Reproduced with permission from [75]. Copyright © 2011, Elsevier

>600 nm. The HIP treatment led to an increase in grain size. The increase in grain size after the HIP processing was simply based on the grain size of the samples after the natural sintering. For a given natural sintering temperature, the variation in the HIP condition had relatively less effect on the grain size as compared with that of the natural sintering.

Figure 7.16 shows relative densities of the samples [75]. It was observed that the effect of the natural sintering temperature was also quite obvious. At the same HIP condition, the higher the natural sintering temperature, the weaker the effect of HIP on the relative density would be. The samples naturally sintered at 1170 and 1185 °C followed by HIP at 1180 °C for 3 h and the sample sintered at 1200 °C followed by HIP at 1180 °C for 5 h exhibited almost the same relative density of 0.9985, while the different in their grain sizes was quite large, i.e., between 580 and 1300 nm. Therefore, this achievement implies that high relative densities can be realized, while grain growth can be well controlled at the same time. It is believed to be also applicable to other transparent ceramic materials.

Highly transparent 8 mol% Y_2O_3–ZrO_2 (8YSZ) ceramics were fabricated by an improved hot isostatic pressing method [92]. Combined with presintering treatment, microstructures, such as positional difference in residual pores, inter-, or intragranular pores, of the 8YSZ ceramics could be well controlled. Commercially available 8 mol% Y_2O_3–ZrO_2 powder was used as a starting material. Green bodies were formed by using cold isostatic pressing method. Pellets with diameter of 20 mm and thickness of 3 mm were made by die pressing at 50 MPa and then isostatically cold-pressed at 200 MPa. The green bodies were presintered in an

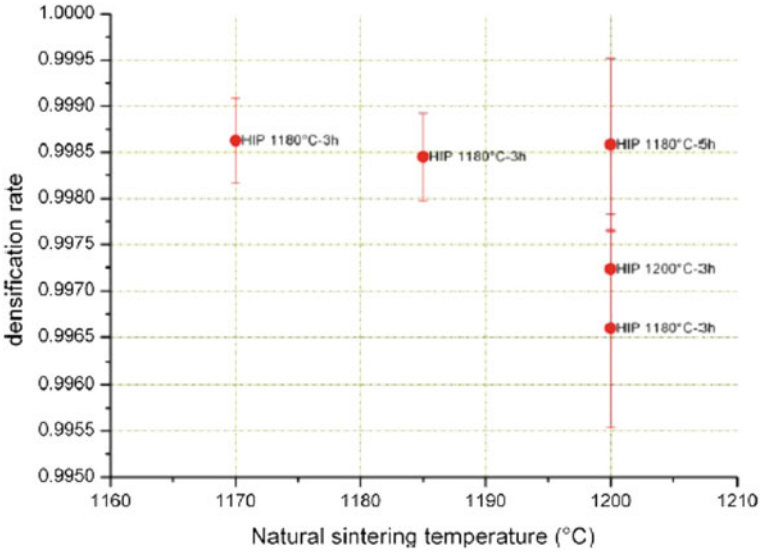

Fig. 7.16 Relative density (τ) after HIP treatment versus the natural sintering temperature. The HIP parameters are indicated for each data. Reproduced with permission from [75]. Copyright © 2011, Elsevier

alumina tube furnace in air. The heating rate was 100 °C h^{-1}, and the holding time was 2 h at temperatures of <1650 °C. The presintered samples were finally treated by using hot isostatic pressing, at temperatures of 1350–1750 °C for 1 h in argon gas at pressure of 150 MPa. The temperature and pressure were simultaneously raised at a heating rate of 500 °C h^{-1}.

According to the experimental results, a microstructure model for pore elimination during the hot isostatic pressing has been proposed to illustrate microstructural evolution of a green body, as shown in Fig. 7.17 [92]. At low presintering temperatures, small intergranular pores are surrounded with fine grains. The intergranular pores transform to intragranular ones when the presintering temperatures are sufficiently high to facilitate grain growth. It is suggested that such intergranular pores are easily removed during the hot isostatic pressing. On the one hand, fine grains have large plastic deformability, which is favorite for pores to shrink at the hot isostatic pressures [93]. On the other hand, it is well known that high-temperature plastic deformability is increased with decreasing grain size [94, 95]. Also, the rapid migration closed gas is through grain boundaries. Small grain size means more grain boundaries, thus being beneficial to the shrinkage of pores. The model has been found to be applicable to many other oxide ceramics [96, 97].

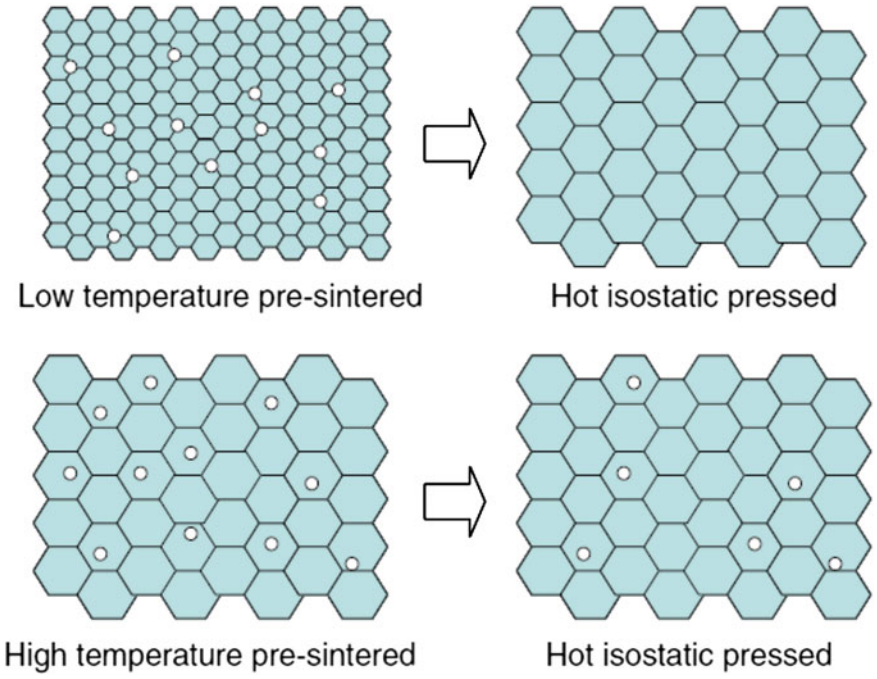

Fig. 7.17 Microstructure model for pore elimination during the sintering of hot isostatic pressing. Reproduced with permission from [92]. Copyright © 2008, John Wiley & Sons

The feasibility of HIP can be further demonstrated by the following examples. Fully dense transparent garnet ceramics were derived cold-pressed green bodies that were subsequently vacuum sintered, with residual porosity being removed by hot isostatic pressing [98]. It was reported that hot isostatic pressing (HIPing) could be used to enhance the electrical and optical properties of PNNZT (50.0/15.5/34.5) [99]. After hot isostatic pressing at 1100 °C, the density was increased to >99 %. Transparent mullite ceramics could be obtained by pressureless sintered combined with hot isostatically pressed (HIP) [100]. In the HIPed mullite, with porosity of <1 %, a transmittance of 40 % was observed in the VIS range and up to 80 % in NIR. Transparent Yb:CaF_2 ceramics could be fabricated by sintering and hot-pressing powders that were derived by a soft chemistry process [101]. There are also reports to use HIP process to consolidate hydroxyapatite (HAp) filter-cakes [102]. HAp ceramics were fully densified at 800 °C after 2 h when a hot isostatic pressure of 100 MPa was used. Besides, transparent α-sialon ceramics [103], transparent magnesium oxide (MgO) ceramics [104], and transparent $La_2Hf_2O_7$ (LHO) ceramics [105] were also fabricated by using HIP process.

7.5 SPS Processed Transparent Ceramics

Various transparent ceramics, such as alumina (Al_2O_3) [106–112], yttrium aluminum garnet (YAG) [113, 114], sesquioxides [115–120], ZrO_2 [121–123], MgO [124], $MgAl_2O_4$ [125–127], mullite [128, 129], hydroxyapatite (HAp) [130, 131], other complex oxide compunds [132], and nonoxides (e.g., AlN) [133], have been processed by using SPS. Also, SPS has been demonstrated to be an effect method to fabricate electro-optic ceramics, including lanthanum-doped lead zirconate stannate titanate (PLZSnT) antiferroelectric ceramics, $PbZrO_3$–$PbTiO_3$–$Pb(Zn_{1/3}Nb_{2/3})O_3$ (PZ–PT–PZN) ferroelectric ceramics [134], and lanthanum-doped lead zirconate titanate ($Pb_{0.92}La_{0.08}(Zr_{0.65}Ti_{0.35})_{0.98}O_3$, PLZT) ceramics [135]. Processing of these transparent ceramics by using the conventional sintering is a significant challenge, due to the content of volatile element (Pb). More recently, transparent $BaTiO_3$ and $SrTiO_3$ ceramics, as well as their solid solutions, $Ba_{1-x}Sr_xTiO_3$ (or BST in short), which can never be obtained by using the conventional sintering techniques, have been achieved by using SPS [136, 137].

The effects of SPS processing parameters on microstructure and optical performance of Al_2O_3 ceramics have been studied [138]. Commercial α-Al_2O_3 powder, with a purity of 99.99 % and an average particle size of 0.15 μm, was used directly in this study. Compacted samples were heated to 1150 °C at a uniaxial pressure of 80 MPa by using a SPS machine (SPS-1050, Sumitomo) with a pulse duration of 3.4 ms. Heating was conducted in a sequent way, with twelve DC pulses (40.8 ms) followed by zero current for 6.8 ms. The heating rate from 600 to 1150 °C was varied between 2 and 100 °C min^{-1}. Temperature was measured with an optical pyrometer focused on a nonthrough hole (1 mm in diameter and 2 mm in depth) of the graphite die. After holding for 20 min at the sintering temperature and subsequent annealing at

1000 °C for 10 min, the sintered disk was about 30 mm in diameter and 3 mm in thickness. In addition, for the heating rates of 8 and 50 °C min^{-1}, sintering time was varied between 0 and 5 h, in order to examine the grain growth behavior. The mechanical pressure was unloaded before annealing.

It was found that, with the sintering parameters stated above, grain size of the final products increased with increasing heating rate. For example, the sample heated at 10 °C min^{-1} had an average grain size of 0.29 μm, while the one heated at 100 °C min^{-1} showed a grain size of 0.55 μm. SEM images of representative samples are shown in Fig. 7.18 [138]. This observation is in contrast to common trend in conventional furnace sintering. It was attributed to the high defect concentration produced by rapid heating and the associated rapid deformation during densification. The defects produced by both rapid heating and deformation would be responsible for the accelerated grain growth, which was further demonstrated in Fig. 7.19. As the temperature just reached 1150 °C, the two heating rates led to samples with almost the same grain size. However, as the sintering time was increased, the grain size of the sample sintered at 50 °C min^{-1} became much larger

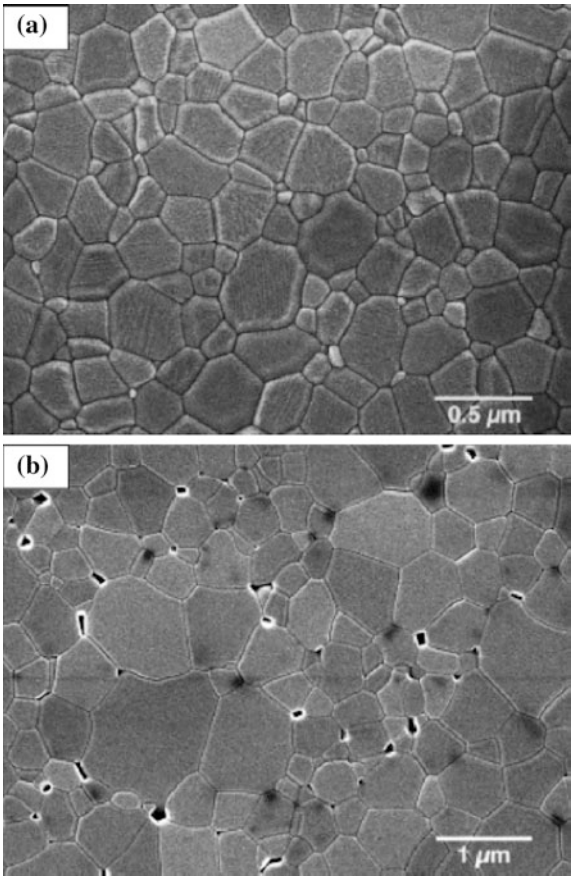

Fig. 7.18 Microstructures of the alumina sintered at a heating rate of **a** 2 °C min^{-1} and **b** 100 °C min^{-1}. Reproduced with permission from [138]. Copyright © 2009, Elsevier

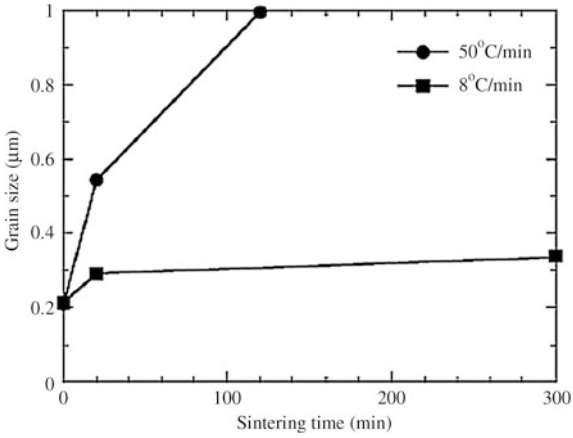

Fig. 7.19 Grain growth behaviors at 1150 °C for two different heating rates. Reproduced with permission from [138]. Copyright © 2009, Elsevier

than that of the one sintered at 8 °C min^{-1}. The effect of heating rate on porosity was normal, i.e., porosity increased with increasing heating rate.

Figure 7.20 shows photographs of the Al_2O_3 ceramics sintered at 1150 °C for 20 m with different heating rates, while tier in-line transmission curves are shown in Fig. 7.21 [138]. It is clearly demonstrated that the heating rate should be as low as possible in order to achieve high optical transparency. However, in practice, a trade-off is necessary, because low heating rate means high energy consumption.

SPS technique even can be used to fabricate samples with special shapes, such as hemispherical domes. For instance, transparent polycrystalline alumina domes have been obtained by combining sintering and forming into one step in minutes [139]. In contrast, fabrication of such items by using the convention sintering technology requires hours. Therefore, SPS provides an unprecedented opportunity to make optically transparent domes at much lower cost, in this respect. In addition, alumina transparent ceramics processed by using SPS have relatively finer grains, due to the rapid heating rate and short sintering time duration.

It is possible to further optimize the sintering effectiveness and efficiency when using SPS. For example, a two-step pressure profile was used to demonstrate the feasibility of SPS in processing $MgAl_2O_4$ [140]. At a low preload pressure, 5 MPa, with a normal fast heating rate of 100 °C min^{-1}, samples could have high in-line transmittance of 51 % at 550 nm and 85 % at 2000 nm. Sintering was carried out in

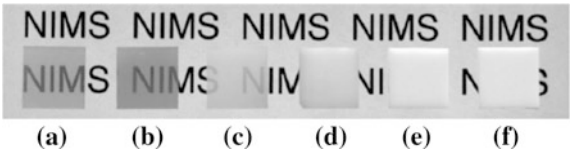

Fig. 7.20 Alumina ceramics sintered by SPS at a heating rate of **a** 2 °C min^{-1}, **b** 5 °C min^{-1}, **c** 10 °C min^{-1}, **d** 25 °C min^{-1}, **e** 50 °C min^{-1}, and **f** 100 °C min^{-1}. All samples are 0.9 mm thick and are put on a transparent polystyrene plate 24 mm above the text. Reproduced with permission from [138]. Copyright © 2009, Elsevier

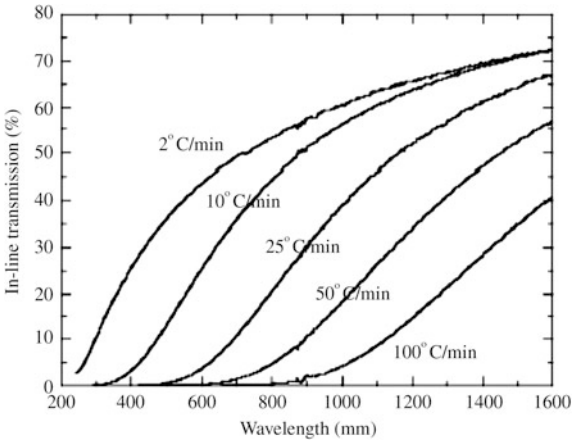

Fig. 7.21 In-line transmission of the alumina sintered at 1150 °C for 20 min. The sample thickness is about 0.9 mm. Reproduced with permission from [138]. Copyright © 2009, Elsevier

vacuum (4–6 Pa) with a Dr. Sinter 2050 SPS apparatus (Sumitomo Coal Mining Company Ltd., Japan). The temperature was increased to 600 °C within 3 min and then further increased to 1250 °C in 6 min, while the final sintering temperature of 1300 °C was reached in 1 min. The sintering time at the final stage for all experiments was 3 min. Five preload pressures, i.e., P_1 = 5, 10, 20, 30, 50, and 100 MPa, were used in the experiment. Photographs of the samples are shown in Fig. 7.22. Obviously, the samples prepared at P_1 of 30, 50, and 100 MPa have a darker discoloration core of about 8 mm in size at their center [140]. The discoloration was attributed to the dislocations formed during the fast densification. Figure 7.23 shows in-line transmittance curves of the samples. It was concluded that a preload

Fig. 7.22 Photographs of the transparent $MgAl_2O_4$ ceramics sintered at 1300 °C for 3 min at different preloaded pressures (P_1): 5 MPa (1.79 mm), 10 MPa (1.99 mm), 20 MPa (1.82 mm), 30 MPa (1.89 mm), 50 MPa (1.82 mm), and 100 MPa (1.60 mm). The samples were 15 mm above the paper, and thicknesses of the samples are indicated in parentheses. Reproduced with permission from [140]. Copyright © 2009, Elsevier

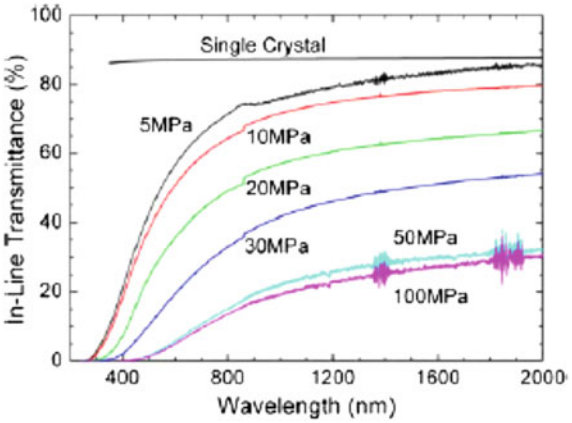

Fig. 7.23 In-line transmittance spectra of the polycrystalline $MgAl_2O_4$ sintered by SPS at different preload pressures P1. The theoretical transmittance of a single-crystal $MgAl_2O_4$ was calculated based on the refraction index as a function of wavelength. Reproduced with permission from [140]. Copyright © 2009, Elsevier

pressure P_1 should not be >20 MPa, so as to obtain acceptable optical transmittance approaching the theoretical limit in the wavelength range of >1000 nm.

Figure 7.24 shows SEM image of the samples processed at 5 MPa and 100 MPa [140]. It was found that both samples exhibited uniform microstructures, which implied that the application of a prepressure had no significant effect on microstructure of the final product. No residual pores were observed on surface the thermally etched sample, while only a very few pores were found by using TEM observation. Average grain sizes of the 5 and 100 MPa samples were 600–700 nm. No significant difference in grain size was observed between the discoloration center and the clean rim. It was attributed to the fact that the temperature gradient was <30 °C in the 12 mm graphite die in the experiment, which was not sufficiently large to lead to energy difference, so that the grain size was not affected.

Transparent Y_2O_3 ceramics have been fabricated by using SPS at moderate temperature and pressure [119]. It was found that sintering temperature had a significant effect on densification, microstructure, optical, and mechanical properties of the Y_2O_3 ceramics. Very high-purity Y_2O_3 powder (99.999 %) was used as the starting material. Before SPS processing, the powder was ball milled in ethanol with ZrO_2 balls for 12 h and then calcined at 1273 K in air for 7.2 ks. SPS-210 LX model SPS setup was used to densify the Y_2O_3 powder. The temperature was first increased to 873 K in 180 s and to 1373 K in 300 s and then held for 300 s. After that, the temperature was further increased to 1373–1823 K at a heating rate of 0.17 K s^{-1} and maintained at each temperature for 2.7 ks. A pressure of 10 MPa was preloaded between room temperature and 1373 K, which was increased to 100 MPa at >1373 K for final sintering. Post-annealing was carried out at 1123–1423 K for 21.6 ks in air.

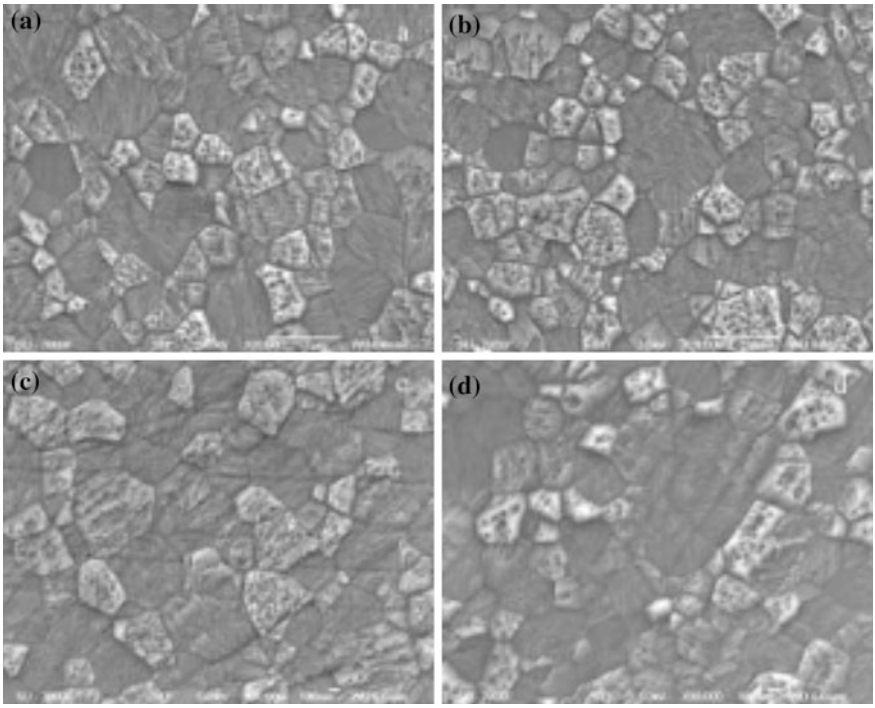

Fig. 7.24 The microstructure of transparent $MgAl_2O_4$ sintered by SPS at 1300 °C for 3 min at different pressures of P1: **a** and **b** 5 MPa and **c** and **d** 100 MPa. **a** and **c** SEM images taken near edge of the samples. **b** and **d** SEM images taken at the discolored center. Reproduced with permission from [140]. Copyright © 2009, Elsevier

Relative density of the sample was 98 % after sintering at 1373 K, while fully dense ceramics with relative density of above 99 % were achieved after sintering at 1473–1823 K. The average grain size was slightly increased from 0.24 to 0.32 μm as the sintering temperature was increased from 1473 to 1573 K. After sintering at 1823 K, the grain size was increased to 1.97 μm [119].

Transmittance spectra of the Y_2O_3 ceramics SPS sintered at 1573 K before and after annealing at 1123–1423 K for 21.6 ks are shown in Fig. 7.25 [119]. As the annealing temperature was increased, transmittance of the samples was increased gradually. The optimized annealing temperature was 1323 K, as shown in Fig. 7.25b. The ultraviolet absorption edge was blue-shifted from 308 to 256 nm, as the annealing temperature was increased from 1123 to 1223 K. No significant change was observed after annealing at higher temperatures of up to 1423 K.

Figure 7.26 shows transmittance spectra of Y_2O_3 bodies sintered at 1473–1773 K after annealing at 1323 K for 21.6 ks in air, together with those that were calculated with the refractive index of Y_2O_3 single crystal [119]. Transmittance of the Y_2O_3 ceramics was increased greatly after annealing. The sample sintered at 1573 K exhibited highest transmittance of 55.0 and 81.7 % at $\lambda = 550$ and 2000 nm.

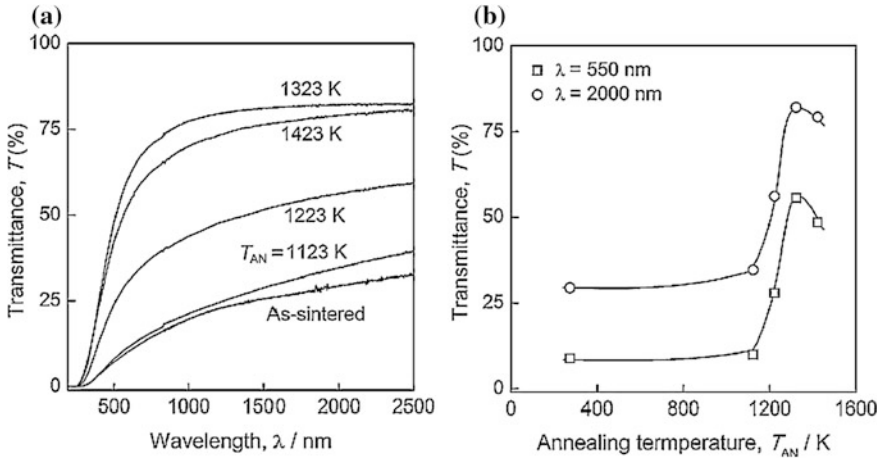

Fig. 7.25 **a** Transmittance spectra of the Y_2O_3 ceramics before and after annealing at 1123–1423 K for 21.6 ks using the samples sintered at 1573 K. **b** Transmittance at λ = 550 and 2000 nm as a function of annealing temperature. Reproduced with permission from [119]. Copyright © 2012, Elsevier

The one sintered at 1573 K after annealing reached nearly 99 % of the theoretical value in the infrared region, as shown in Fig. 7.26a. This temperature was much lower than those required by other sintering techniques.

Vickers hardness (H_V) and fracture toughness of the annealed Y_2O_3 ceramics as a function of sintering temperature are shown in Fig. 7.27a, while relationship between H_V and grain size is illustrated in Fig. 7.27b [119]. H_V of the Y_2O_3 ceramics sintered

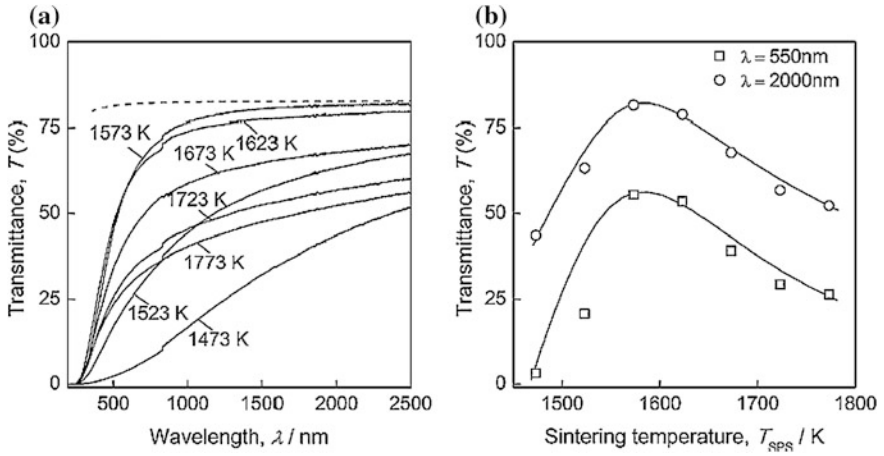

Fig. 7.26 **a** Transmittance spectra of the Y_2O_3 ceramics sintered at 1473–1773 K after annealing at 1323 K. **b** Transmittance at λ = 550 and 2000 nm as a function of sintering temperature. The dashed line indicates transmittance calculated from the refractive index of Y_2O_3 single crystal. Reproduced with permission from [119]. Copyright © 2012, Elsevier

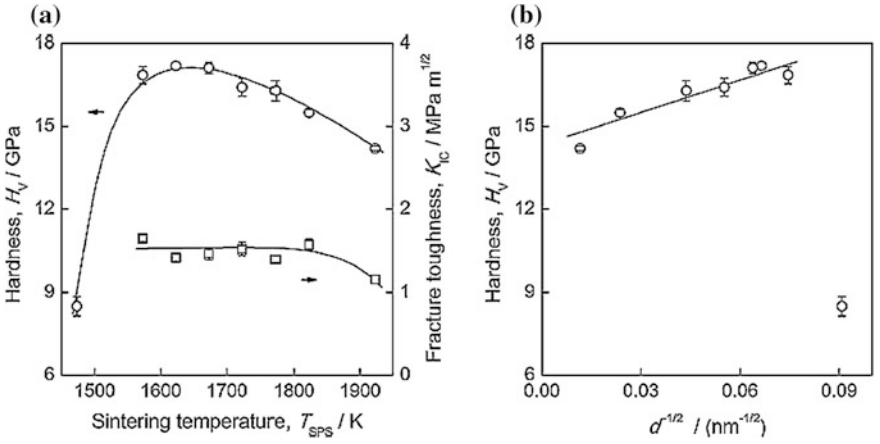

Fig. 7.27 **a** Vickers hardness and fracture toughness of the Y_2O_3 ceramics annealed at 1323 K as a function of sintering temperature. **b** Vickers hardness as a function of the inverse square root of grain size. Reproduced with permission from [119]. Copyright © 2012, Elsevier

at 1373 K was 8.3 GPa. It was sharply increased to ~17.2 GPa after sintering at 1573 K. A maximum value of ~17.5 GPa was achieved at the sintering temperature of 1623 K. After that, the value of H_V steadily decreased to ~14 GPa after sintering at 1923 K. Fracture toughness was in the range of 1.0–1.5 MPa m$^{1/2}$, which was not significantly influenced by sintering temperature, especially over 1573–1823 K. H_V of the Y_2O_3 ceramics showed a linear relationship with $d^{-1/2}$, i.e., the Hall–Petch relation. The fact that H_V increases with $d^{-1/2}$ in ceramics has been explained in terms of the reduced free path for dislocations as the grain size is decreased [141].

Transparent YAG ceramics have been fabricated by using SPS (Dr. Sinter 2050) and commercial YAG powder as starting material [114]. The YAG powder was of nonagglomerated spherical shaped particles with average particle diameter of 34 ± 17 nm and lognormal particle size distribution. Graphite foils (Grafoil) were used as spacers between the sample to be sintered and the graphite die and the punches. A preloaded pressure of 100 MPa was applied before the heating was started. The pressure was maintained during the whole heating process and at the SPS temperatures during the sintering. The temperature was increased to 600 °C within 3 min, after which it was raised to sintering temperatures at a heating rate of 100 °C min^{-1}.

During the densification of nanocrystalline powder compacts by using cold pressing, it is very common that large pores could be entrapped, due to the agglomeration of the fine particles. Remove of such pores during pressureless sintering and densification is quite difficult, due to the presence of the junctions with high dihedral angles at the pore–grain boundaries. However, the SPS compact of YAG at 900 °C exhibited particles with homogeneous distribution and pores with comparable size with the particle sizes, as shown in Fig. 7.28 [114]. This was mainly because the YAG powder had no agglomeration. Such homogeneous and

small pore size could not result in full densification when using pressureless sintering, because many pores had high coordination numbers. However, this problem could be addressed by using SPS, due to the application of pressures. Pressures would assist the closure of such pores through grain sliding.

Figure 7.29 shows SEM images of the samples sintered at higher temperatures [114]. The sample sintered at 1250 °C was still opaque, while the one sintered at 1400 °C had been transparent. Both samples showed homogeneous microstructure. Relative density of the YAG samples was increased significantly from 83 to 99.6 %, although the temperature range was as narrow as 150 °C. Grain size in this temperature range was increased in a parabolic manner. Significant grain growth was observed at the temperatures of above 1400 °C. The grain growth behaviors below and above 1400 °C were different [114].

SPS time duration had effect on densification and grain growth of YAG ceramics. For example, as the SPS duration was increased from 3 to 6 min, the relative density was increased tremendously, especially at lower temperatures, e.g., <1300 °C, as shown in Fig. 7.30 [114]. Therefore, if the sintering duration was

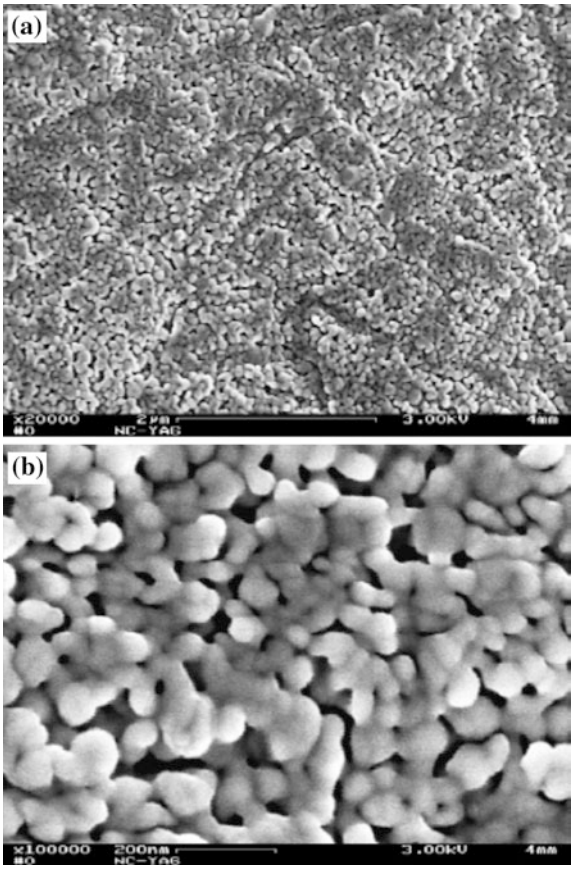

Fig. 7.28 Low (**a**) and high (**b**) magnification SEM images of the samples derived from the YAG compact subjected to SPS for 3 min at 900 °C and 100 MPa, which were further annealed at 900 °C for 5 h. Homogeneous distribution of the particles and pores with comparable sizes could be observed. Reproduced with permission from [114]. Copyright © 2007, Elsevier

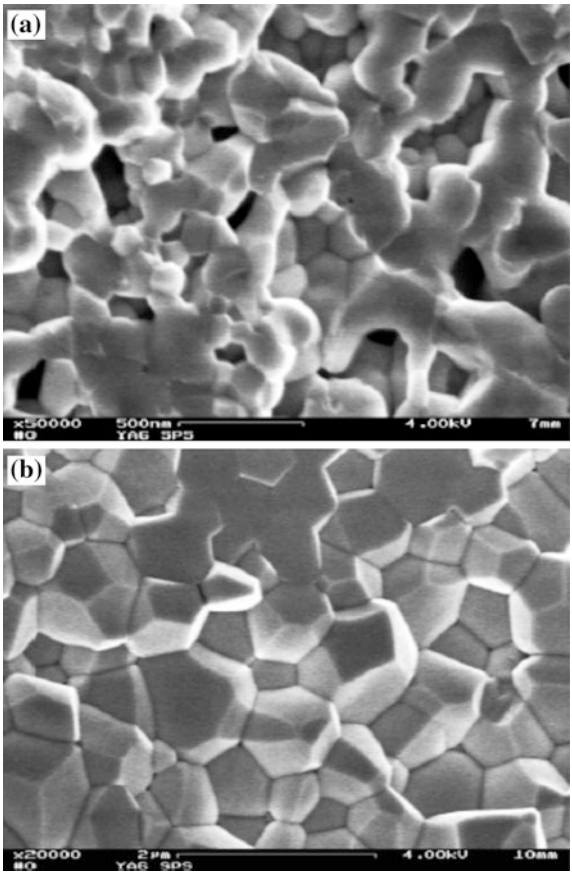

Fig. 7.29 SEM images of fracture surfaces of YAG ceramics after SPS for 3 min at 100 MPa at different temperatures: **a** 1250 °C and **b** 1450 °C. Reproduced with permission from [114]. Copyright © 2007, Elsevier

increased from 3 to 6 min, the sintering temperature could be reduced by about 75 °C, for a given relative density. After 6 min sintering at 1350 °C, transparent YAG ceramics could be obtained. It was worth mentioning that the sample sintered for 6 min at 1300 °C had higher density than the one sintered to 3 min at 1350 °C, which indicated the negative effect of grain growth on densification during SPS. In this case, the densification was governed by the atomic transport processes at surface of the particles and particle–particle interfaces. Densification and grain growth by grain rotation and sliding would convert the originally high-angle grain boundaries to low-angle grain boundaries that in turn are annealed out by short-circuit diffusion. TEM observations verified the presence of such low-angle grain boundaries in dense ceramics was confirmed by TEM analysis, as shown in Fig. 7.31 [114]. In addition, Fig. 7.30 also indicated the effect of pressure.

In another study, it was found that the way to treat the precursor powder had significant effect on performance of YAG ceramics by using SPS [142]. When sintering YAG synthesised by using reverse-strike co-precipitation with SPS, the precursor powder was calcined at 1000 °C and dispersed by using ball milling with

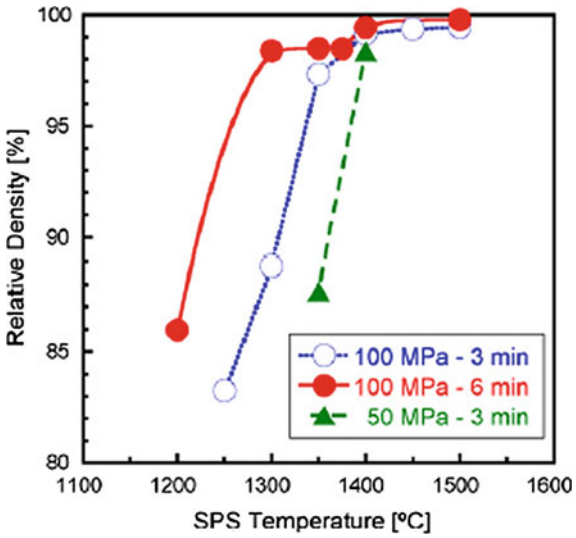

Fig. 7.30 Relative density of the YAG powder compacts after SPS for 3 and 6 min at 50 and 100 MPa, as a function sintering temperature. Reproduced with permission from [114]. Copyright © 2007, Elsevier

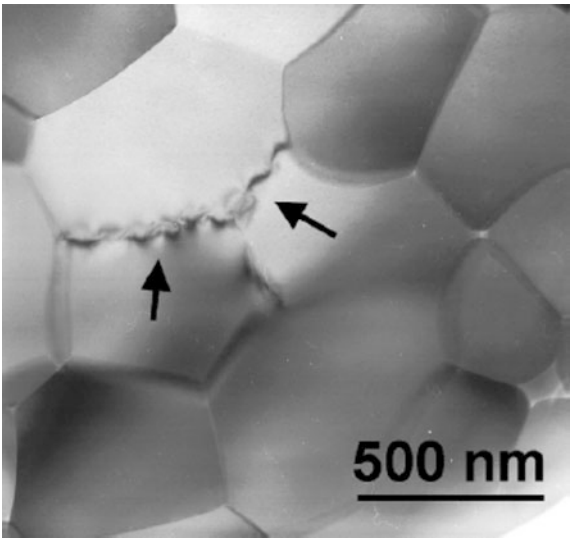

Fig. 7.31 TEM image of the YAG ceramics after SPS for 3 min at 1400 °C and 100 MPa. The high-angle grain boundaries appeared as straight lines. The low-angle grain boundaries (*arrowed*) appeared to be curvy due to the strain field caused by dislocations. Nanometer-sized residual pores were present at the grain-boundary junctions. Reproduced with permission from [114]. Copyright © 2007, Elsevier

α-alumina (BM_A) or zirconia (BMz) balls or ultrasonication (US). All the three dispersed powders could be consolidated by using SPS to nearly theoretical density, but only the US powder was optically transparent, as shown in Fig. 7.32.

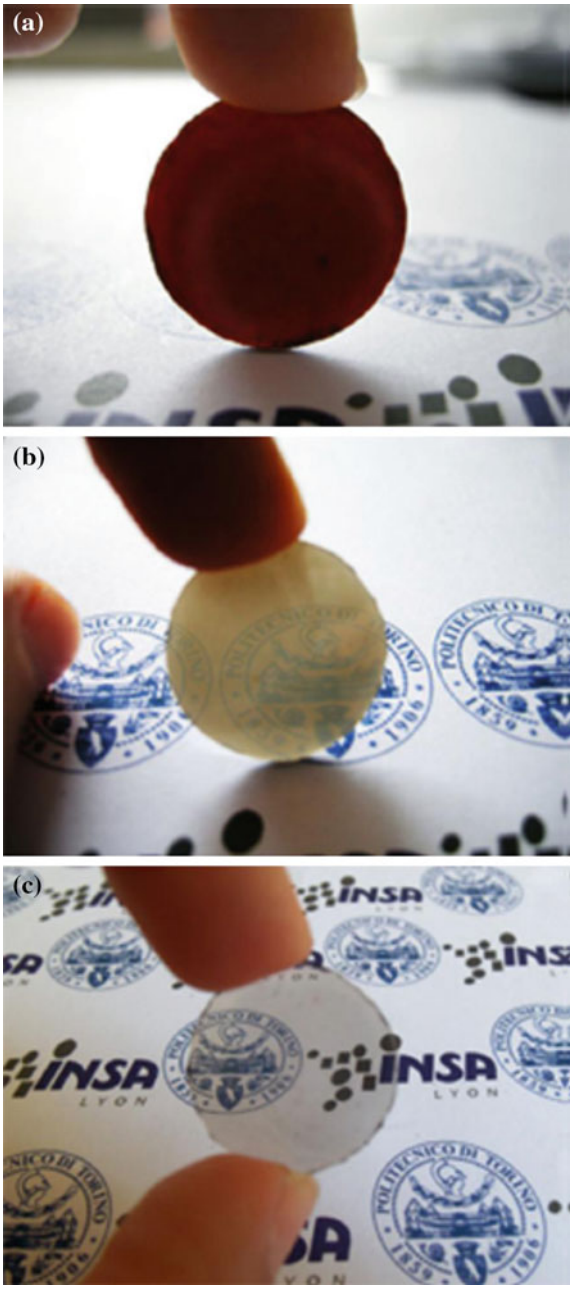

Fig. 7.32 Photographs of the samples derived from powders of BM_Z (**a**), BM_A (**b**), and US (**c**) after thermal annealing. Reproduced with permission from [142]. Copyright © 2013, Elsevier

The 1-mm-thick transparent sample possessed a transmittance of about 60 % at 600 nm. According to Raman spectroscopy, it was found that there were some phonon vibrational shifts, which implied that minor secondary phases could be have introduced due to the contamination from the milling media. Such minor secondary phases could not be detectable by using XRD, because of their very small quantity. This result further indicates that special carefulness is important when processing transparent ceramics.

Recently, SPS has been used to prepare pyrochlore transparent ceramics, including $Lu_2Ti_2O_7$ [143, 144], $Lu_2Hf_2O_7$ [145], and Lu_3NbO_7 [146, 147], which is still a challenge by using other sintering techniques. Figure 7.33 shows photograph and transmittance curves of transparent $Lu_2Ti_2O_7$ pyrochlore ceramics, which was synthesized by using SPS through reactive sintering directly from Lu_2O_3 and TiO_2 oxide precursors at 1723 K for 45 min [143]. The annealed ceramics demonstrated a transmittance of 72 % at wavelength of 2000 nm and 40 % transmittance at 550 nm. The average grain size was 14.5 μm with uniform microstructure. Representative results of Lu_3NbO_7 transparent ceramics, fabricated by using SPS, are shown in Figs. 7.34 and 7.35 [147].

Another distinctive advantage of SPS is its ability to processing the transparent ceramics containing elements that are unstable in air, such as nitrogen (N), phosphorus (P), and fluorine (F). Examples include AlON [148] and Yb^{3+}-doped $Sr_5(PO_4)_3F$ [149]. More significantly, $Sr_5(PO_4)_3F$ is a hexagonal crystal, instead of cubic ones as required according to the general understanding on transparent ceramics, as discussed previously. 20 mol% Yb^{3+}-doped $Sr_5(PO_4)_3F$ nanopowder was synthesized by using a co-precipitation method, with $Sr(NO_3)_2$, $Yb(NO_3)_3$, $(NH4)_2HPO_4$, and NH_4F as starting materials [149]. Solution containing 0.03 M Sr $(NO_3)_2$ and 0.0013 M $Yb(NO_3)_3$ was mixed with solution of 0.013 M NH_4F and 0.04 M $(NH_4)_2HPO_4$ to precipitate the precursor particles. The powder was ball milled for 20 h using ethanol as a solvent first and then dried at 70 °C and sieved

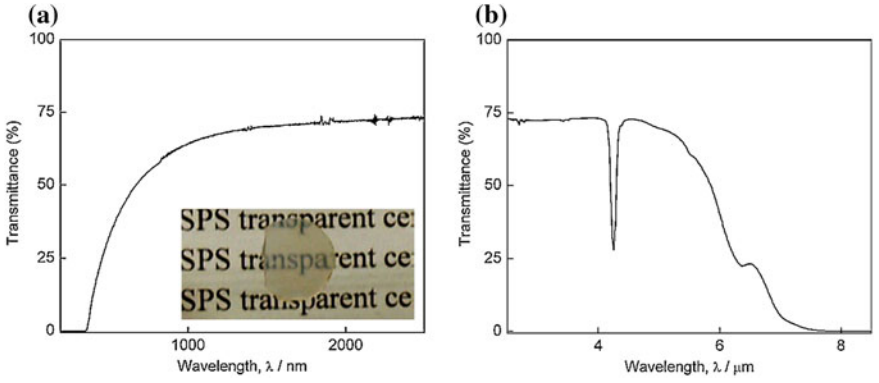

Fig. 7.33 Transmittance spectra of $Lu_2Ti_2O_7$ sintered at 1723 K for 45 min in different ranges: **a** 190–2500 nm and **b** 2.5–8.5 μm. The inset is photograph of the transparent ceramics. Reproduced with permission from [143]. Copyright © 2011, Elsevier

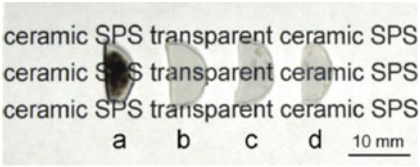

Fig. 7.34 Photographs of the Lu_3NbO_7 ceramics SPS sintered at 1500 °C and annealed at various temperatures in air for 6 h: **a** 750 °C, **b** 850 °C, **c** 950 °C, and **d** 1050 °C. Reproduced with permission from [147]. Copyright © 2013, Elsevier

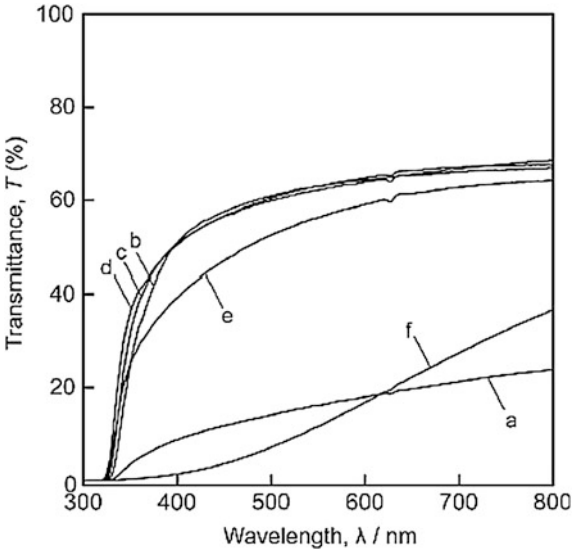

Fig. 7.35 Transmittance curves of the Lu_3NbO_7 ceramics SPS sintered at 1450 °C and annealed at various temperatures in air for 6 h: **a** 750 °C, **b** 850 °C, **c** 950 °C, **d** 1050 °C, **e** 1150 °C, and **f** 1250 °C. Reproduced with permission from [147]. Copyright © 2013, Elsevier

with a 200 mesh screen. The powder was finally put into graphite mold and then separated by foil and BN spraying coatings from the mold. The sample was sintered in a FCT System SPS facility, at a heating rate of 50 °C min^{-1} from RT to 1050 °C at a loading pressure of 100 MPa for 8 min. A trance of second phase, $Sr_9Yb(PO_4)_7$, was found in the sintered ceramics, which could be suppressed by using a small amount of SrF_2.

Photographs of representative Yb^{3+}-doped $Sr_5(PO_4)_3F$ transparent ceramics are shown in Fig. 7.36 [149]. A TEM image of the ceramics is also included in the figure. It was found that almost no porosity could be observed in the SPS-sintered sample. The grain sizes were ranged from 40 to 200 nm, with an average value of about 150 nm. In-line optical transmittance spectrum indicated that the $Sr_5(PO_4)_3F$: Yb ceramics had a strong absorption in the range of 850–980 nm, showing high potential to be high-power laser material. The transmittance near the emission wavelength was above 74 % at 1000 nm.

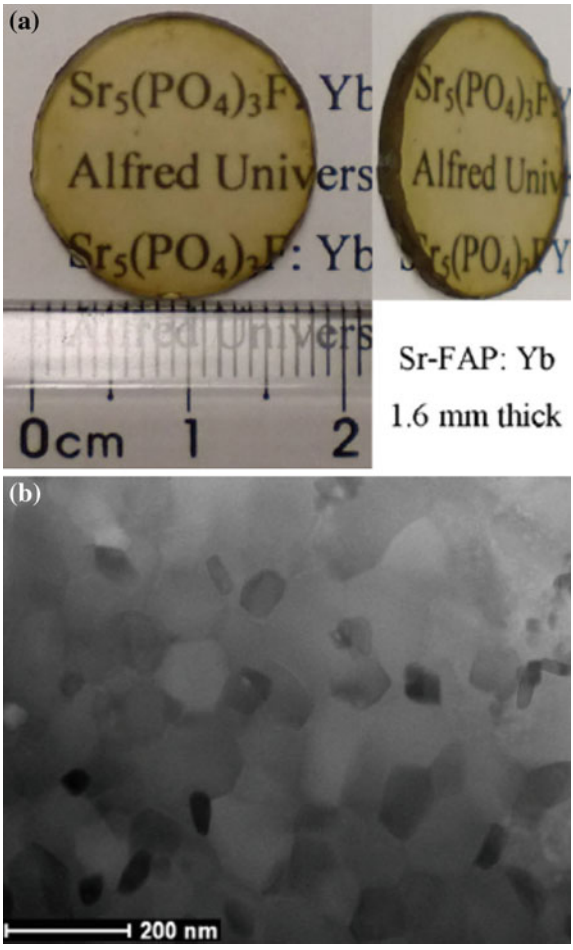

Fig. 7.36 Photographs (*top*) and TEM image (*bottom*) of the Yb^{3+}-doped $Sr_5(PO_4)_3F$ transparent ceramics processed by using SPS. Reproduced with permission from [149]. Copyright © 2012, John Wiley & Sons

7.6 MW-Processed Transparent Ceramics

The use of MW sintering to fabricate transparent ceramics is relatively less popular currently. Transparent ceramics that have been processed by using MW sintering include Al_2O_3 [150–152], YAG [153], AlON [154], and mullite [155]. MW sintering has been shown to be an effective technique to produce transparent ceramics as compared with the conventional sintering technologies.

First example discussed in this section is MW-processed Al_2O_3 transparent ceramics reported by Cheng et al. [150]. High-purity (99.99 %) commercial Al_2O_3 powder with average particle size of 0.15 μm was used as precursor. A total of 0.05 wt% of MgO was incorporated through a wet-chemical route with $Mg(NO_3)_2{\cdot}5H_2O$ as sintering promoter. Green pellets, with relative densities of

52–54 %, were prepared by dry pressing uniaxially, followed by cold isostatic pressing at 280 MPa. The compacted pellets were preheated at 1100 °C for 2 h in a resistance furnace to burn out the binder. Microwave sintering was carried out using a TE103 single-mode microwave applicator that was coupled with a 1.5-kW microwave generator operating at 2.45 GHz for small samples with diameters of <12.7 mm and a multi-mode microwave applicator with a 6-kW microwave power source for large samples with diameters of up to 25.4 mm. Ultrahigh-purity hydrogen under ambient pressure was used as sintering atmosphere.

Figure 7.37 shows photograph of a representative transparent Al_2O_3 ceramics that was microwave sintered at 1750 °C for 45 min [150]. In the reported experimental range, optical transmittance of the samples was slightly increased with increasing sintering time. Figure 7.38 shows SEM images of the samples microwave sintered at 1750 °C for different time durations. All samples exhibited uniform microstructure and grain size, with almost 100 % relative density, i.e., 3.97 g cm^{-3}. As the sintering time was increased from 15 to 45 min, the average grain size was increased from 20 to 40 μm.

Some microwave sintered transparent Al_2O_3 samples were post-sintered in microwave field at 1850–1880 °C for 2 h under ultrahigh-purity hydrogen (H_2) atmosphere, in order to convert the polycrystalline ceramics to single crystals. The processing is schematically shown in Fig. 7.39 [150]. A 9.5-mm-diameter Al_2O_3 disk, which was an as-sintered transparent sample by using MW sintering at 1750 °C for 30 min and supported by a high-purity Al_2O_3 tube, was placed in the single-mode microwave cavity to apply microwave post-sintering treatment. It was found that the temperatures at the center and periphery of the Al_2O_3 disk could be slightly different, due to the cooling effect of the flowing H_2 on the peripheral area.

As shown in Fig. 7.40, significant change in microstructure was observed in the post-sintered Al_2O_3 sample that was microwave heated at 1880 °C for 30 min [150]. It was demonstrated that the conversion of the polycrystalline ceramics to single crystal could be achieved by using the microwave post-sintering process. The peripheral area of the sample was still polycrystalline with average grain size of

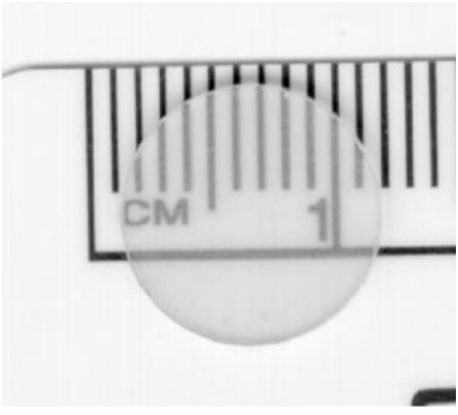

Fig. 7.37 Photograph of a representative highly transparent Al_2O_3 ceramics microwave sintered at 1750 °C for 45 min. Reproduced with permission from [150]. Copyright © 2002, Elsevier

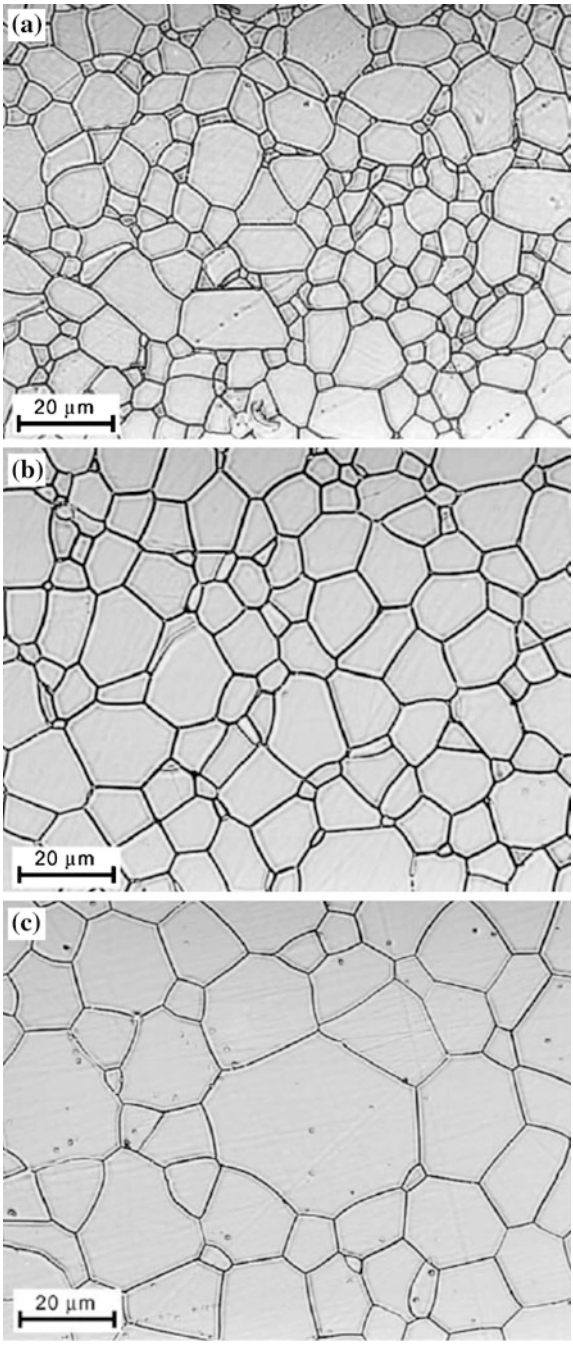

Fig. 7.38 SEM images of the Al_2O_3 ceramics with 0.05 wt% MgO microwave sintered at 1750 °C at a heating rate of 100 °C min^{-1} for different time durations: **a** 15, **b** 30, and **c** 45 min. Reproduced with permission from [150]. Copyright © 2002, Elsevier

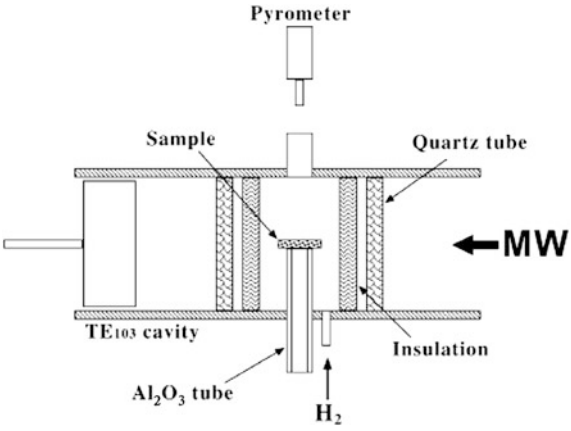

Fig. 7.39 Schematic of the microwave setup for solid-state conversion of polycrystalline Al_2O_3 sample to single-crystal sapphire. Reproduced with permission from [150]. Copyright © 2002, Elsevier

30–40 μm, as shown at the top panel in Fig. 7.40, whereas the center part of the post-sintered sample was converted into single crystal without the presence of grain boundaries, i.e., the bottom panel of the figure. The converted sample exhibited an enhanced transmittance by about 20 % as compared with the as-sintered ones, showing the feasibility and advantage of MW sintering technique.

Another example of transparent Al_2O_3 was fabricated by using microwave sintering at 2.54 GHz [151]. Figure 7.41 shows a schematic diagram of the microwave sintering with a special designed insulating casket. The hole on the top cover was used for infrared pyrometer. SiC powder was used as a microwave absorber, acting as a low-temperature microwave susceptor to preheat the Al_2O_3 samples, because Al_2O_3 is a poor microwave absorber at room temperature.

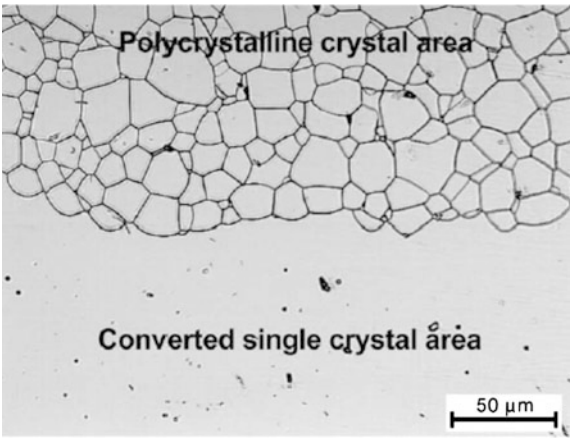

Fig. 7.40 SEM image of the Al_2O_3 sample microwave post-sintered at 1880 °C for 120 min, showing microstructure development due to the conversion of polycrystalline to single-crystal structure. Reproduced with permission from [150]. Copyright © 2002, Elsevier

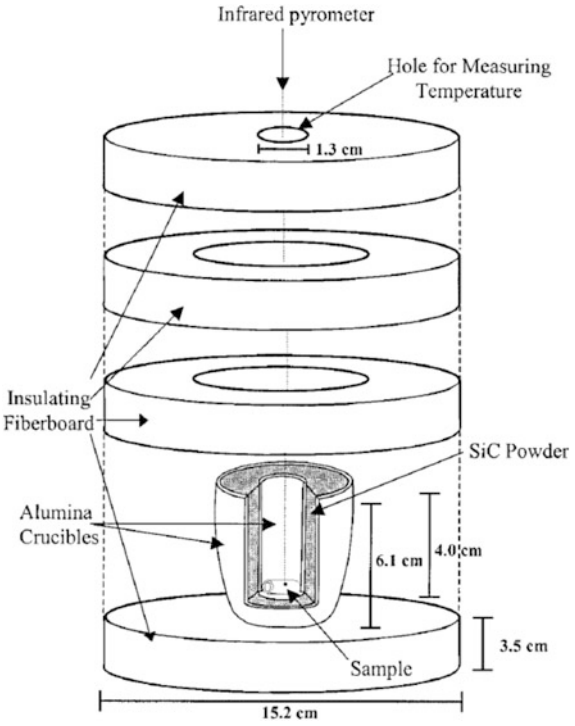

Fig. 7.41 Schematic diagram of a microwave sintering with specially designed insulating casket. Reproduced with permission from [151]. Copyright © 2003, John Wiley & Sons

The precursor alumina powder was doped with 350 ppm Y_2O_3 and 500 ppm MgO. Binder was removed by heating to 650 °C at 5 °C min^{-1} with by using a conventional furnace. The average green density of the tubes after binder removal was 1.63 ± 0.01 g cm^{-3}, i.e., 40.85 ± 0.35 % relative density. A multi-mode 6-kW, 2.45-GHz microwave furnace was used to sintering the samples. The sintering temperature and heating rate of microwave sintering were controlled by adjusting the input power. The sintering temperatures in the microwave furnace were measured by using digital infrared pyrometer.

Figure 7.42 shows density of the samples, for microwave and conventional sintering, as a function of sintering temperature [151]. Without dwelling at the sintering temperatures, microwave sintered Al_2O_3 samples reached relative density of 95 % after sintering at 1350 °C, which was much lower than 1600 °C for the conventionally heated samples. Also, the microwave sintered sample was almost fully densified after sintering at 1400 °C, while the density of the sample sintered through the conventional sintering was only about 50 %. Microwave sintering reduced the temperature for the samples start to densify by about 300 °C.

It was found that both the microwave sintering and the conventional sintering exhibited a similar grain growth behavior, as shown in Fig. 7.43 [151]. Therefore, the enhancement in densification of Al_2O_3 by the microwave sintering was not due to the fast heating rate. However, the microwave densification corresponded to apparent activation energy of 85 ± 10 kJ mol^{-1}, much lower than the value of

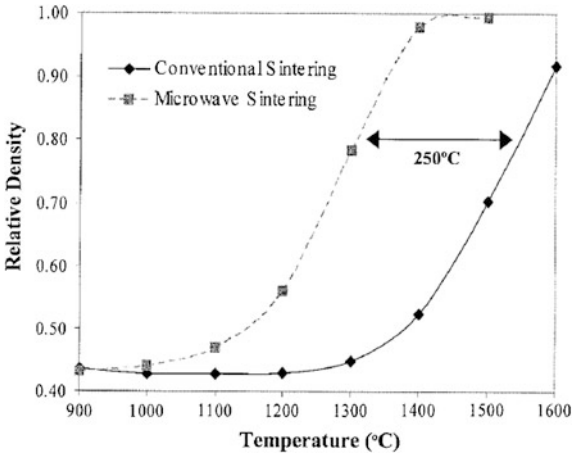

Fig. 7.42 Density of the samples, sintered by using microwave sintering and conventional sintering without holding at the sintering temperature, as a function of sintering temperature. Reproduced with permission from [151]. Copyright © 2003, John Wiley & Sons

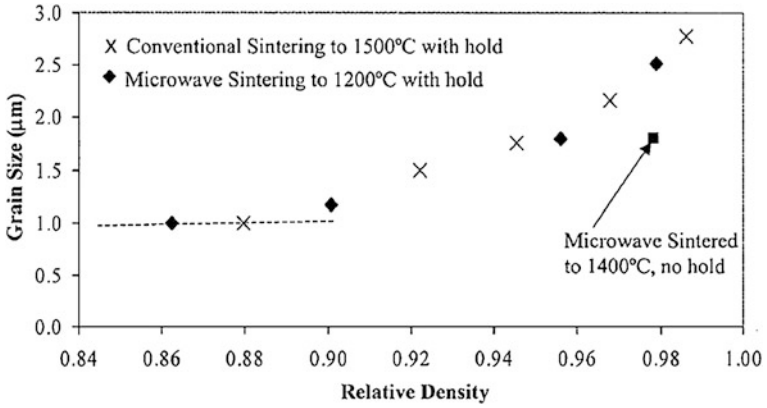

Fig. 7.43 Grain growth trajectories of the microwave sintered and conventionally sintered samples. Reproduced with permission from [151]. Copyright © 2003, John Wiley & Sons

520 ± 14 kJ mol^{-1} for the conventional sintering, meaning that the there was a difference in densification mechanism between the two sintering techniques, which deserves for further investigation.

A gyrotron-based system operating at a frequency of 24 GHz with microwave power up to 6 kW has been used to develop YAG transparent ceramics through reactive sintering from oxide precursors [153]. TEOS with contents of 0.3 and 0.5 wt% was used to provide SiO_2 as sintering aid.

Figure 7.44 shows photograph and microstructure of representative sample [153]. The sample contained 1.0 % Yb and 0.5 wt% TEOS and sintered at 1730 °C

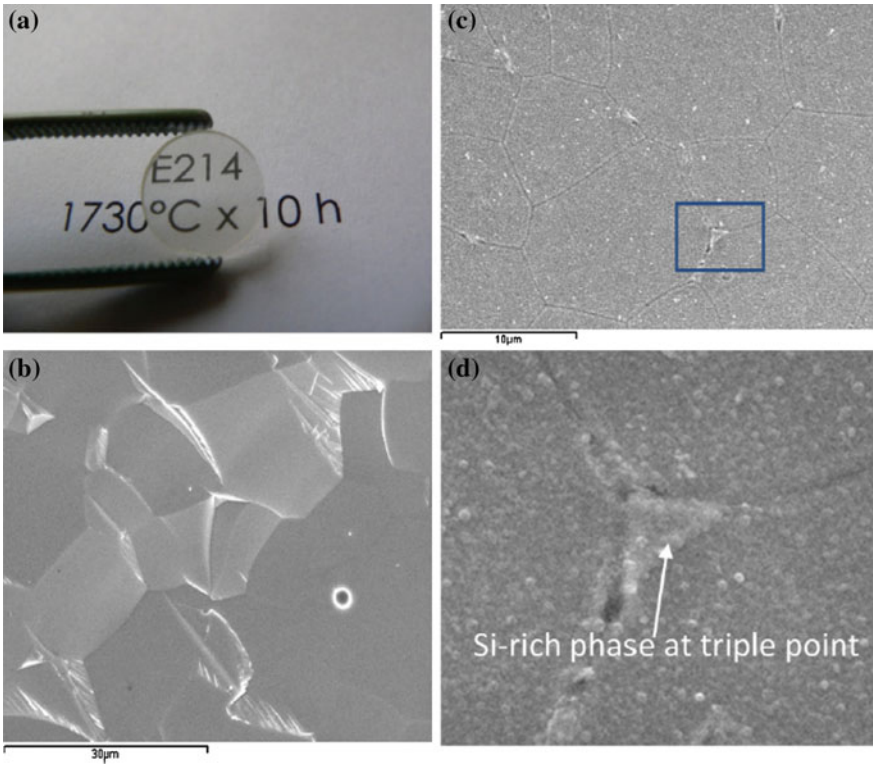

Fig. 7.44 *Photograph* **a** and SEM images of the sample 1.0 % Yb:YAG with 0.5 wt% TOES sintered at 1730 °C for 10 h: **b** fracture surface and **b**, **c** polished and thermally etched surface. Reproduced with permission from [153]. Copyright © 2013, Elsevier

for 10 h. As shown in Fig. 7.44b, on the fracture surface, few pores were observed, most of which were preferentially within the grains. The sample exhibited grain sizes ranging from 5 to 20 μm, as shown by the polished and thermally etched surface in Fig. 7.44c. It was also found that the content of TEOS had no significant effect on grain size of the YAG transparent ceramics. Figure 7.44d indicated that amorphous or crystalline phase enriched with SiO_2 could be found at some triple junctions or grain boundaries. Such phases might have been formed during the thermal etching process, due to the diffusion of silicon through the grains toward the grain boundaries.

As stated previously, the sintering behavior of various transparent ceramics, including YAG, can be improved by using silica-containing sintering aid. In conventional sintering, silica functions to form a liquid phase at about 1390 °C. The liquid phase makes it easier for the particles to rearrange and enhances mass transport by grain-boundary diffusion, so as to promote densification. During cooling from the sintering temperature, secondary phases of Al_2O_3–Y_2O_3–SiO_2,

either amorphous or crystalline, would be formed. The presence of such phases is harmful to optical properties due to their light scattering. Therefore, a trade-off is necessary to optimize the content of silica, i.e., promoting densification yet without compromising optical performances.

One of the most distinctive features of the microwave sintering is that there is a special behavior in microwave power in the initial stage of heating. For example, in that study, there was a drop in microwave power as the temperature was above 700 °C [153]. It was attributed to the increase in microwave absorption of the sample, due to the increase in their ionic conductivity. The microwave power was also influenced by the exothermal reactions of the intermediate $Y_4Al_2O_9$ and $YAlO_3$.

The formation of YAG through solid-state reaction is controlled by the diffusion of Al^{3+} [156]. Such diffusion of Al^{3+} was enhanced by the microwave field, so that the reaction temperature of YAG and its sintering temperature were decreased, as evidenced by the pores entrapped in grains, as shown in Fig. 7.44b. Similarly, the formation of the liquid phase was also promoted. In other words, the content of sintering aids could be reduced when using microwave sintering, which however needs further clarification.

The enhancement in mass transport of polycrystalline materials has been explained by the so-called ponderomotive action of electromagnetic field on charged particles [157, 158]. The theory suggested that the ponderomotive effect is more effective in ionic crystalline materials with high microwave absorption and it is maximized when the imaginary part and real parts of the complex dielectric permittivity of the materials have very close values. It can be expected the microwave processing parameters could be further optimized in such a way that all diffusion processes would be operated concurrently during the densification of powder compacts. In this case, the amount of sintering aids could be greatly reduced or even completely avoided.

Besides, Roy et al. found that single-phase ALON could be synthesized from Al_2O_3 and AlN by using microwave heating at 1650 °C for 1 h, while fully dense and transparent ALON ceramics were obtained through microwave sintering at 1800 °C for 1 h [154]. A total transmission of 60 % was achieved for the polished sample with a thickness of 0.6 mm. The microwave sintering was carried out by using a homemade 1.5-kW, 2.45-GHz single-mode microwave applicator in nitrogen (N_2) flowing at ambient pressure. The heating rate was about 100 °C min^{-1} by controlling the incident microwave power.

Transparent mullite ceramics were developed by using microwave sintering at about 1300 °C [155]. The microwave sintering was conducted by using a 2.45-GHz, 900-W microwave furnace. The samples were heated in the microwave field directly from room temperature to 1300 °C and held at the temperature for 10 min, then allowed to cool down naturally. The results indicated that aerogel of mullite stoichiometry, free of agglomeration and highly active, was key factor to achieving transparent mullite ceramics.

7.7 Concluding Remarks

Vacuum sintering is the most widely used technique to fabricate transparent ceramics, due to its various advantages, such as simple processing, large size product, and relatively cost-effectiveness. HP and HIP offer lower sintering temperatures, so that transparent ceramics with fine-grained microstructures could be obtained, which make them attractive in some applications requiring strong mechanical performances.

References

1. Boulesteix R, Maitre A, Chretien L, Rabinovitch Y, Salle C (2013) Microstructural evolution during vacuum sintering of yttrium aluminum garnet transparent ceramics: toward the origin of residual porosity affecting the transparency. J Am Ceram Soc 96:1724–1731
2. Stevenson AJ, Bittel BC, Leh CG, Li X, Dickey EC, Lenahan PM et al (2011) Color center formation in vacuum sintered $Nd_{3x}Y_{3-3x}Al_5O_{12}$ transparent ceramics. Appl Phys Lett 98:051906
3. Tang F, Cao YG, Huang JQ, Guo W, Liu HG, Huang QF et al (2012) Multilayer YAG/RE: YAG/YAG laser ceramic prepared by tape casting and vacuum sintering method. J Eur Ceram Soc 32:3995–4002
4. Xu J, Shi Y, Xie JJ, Lei F (2013) Fabrication, microstructure, and luminescent properties of Ce^{3+}-Doped $Lu_3Al_5O_{12}$ (Ce:LuAG) transparent ceramics by low-temperature vacuum sintering. J Am Ceram Soc 96:1930–1936
5. Ikesue A, Furusato I, Kamata K (1995) Fabrication of polycrystalline transparent YAG ceramics by a solid-state reaction method. J Am Ceram Soc 78:225–228
6. Ikesue A, Kamata K, Yoshida K (1995) Synthesis of Nd^{3+}, Cr^{3+}-coped YAG ceramics for high-efficiency solid-state lasers. J Am Ceram Soc 78:2545–2547
7. Ikesue A, Kinoshita T, Kamata K, Yoshida K (1995) Fabrication and optical properties of high-performance polycrystalline Nd-YAG ceramics for solid-state lasers. J Am Ceram Soc 78:1033–1040
8. Chang XH, He DW, Zhang J, Zou YT, Wang JH, Lu TC (2010) Effects of vacuum heat treatment of nano powder on sintering of transparent nano-crystalline $MgAl_2O_4$ ceramics. In: Pan W, Gong J, (eds) High-performance ceramics VI. p 657–660
9. Li JG, Ikegami T, Lee JH, Mori T, Yajima Y (2001) A wet-chemical process yielding reactive magnesium aluminate spinel ($MgAl_2O_4$) powder. Ceram Int 27:481–489
10. Sun YF, Lu TC, Wang XJ (2007) Preparation and optical properties of transparent Mn: $MgAl_2O_4$ ceramics. Rare Metal Mater Eng 36:438–441
11. Rozenburg K, Reimanis IE, Kleebe HJ, Cook RL (2008) Sintering kinetics of a $MgAl_2O_4$ spinel doped with LiF. J Am Ceram Soc 91:444–450
12. Mata-Osoro G, Moya JS, Pecharroman C (2012) Transparent alumina by vacuum sintering. J Eur Ceram Soc 32:2925–2933
13. Zhang X, Liang S, Zhang P, Zhao T, Bai Y, Bao CG et al (2012) Fabrication of transparent alumina by rapid vacuum pressureless sintering technology. J Am Ceram Soc 95:2116–2119
14. Li WJ, Zhou SM, Liu N, Lin H, Teng H, Li YK et al (2010) Synthesis and spectral properties of Yb^{3+}/Ho^{3+} co-doped yttria 2 mu m transparent ceramics. Mater Lett 64:1344–1346
15. Wen L, Sun XD, Lu Q, Xu GX, Hu XZ (2006) Synthesis of yttria nanopowders for transparent yttria ceramics. Opt Mater 29:239–245

16. Jin LL, Zhou GH, Shimai S, Zhang J, Wang SW (2010) ZrO_2-doped Y_2O_3 transparent ceramics via slip casting and vacuum sintering. J Eur Ceram Soc 30:2139–2143
17. Huang YH, Jiang DL, Zhang JX, Lin QL (2009) Fabrication of transparent lanthanum-doped yttria ceramics by combination of two-step sintering and vacuum sintering. J Am Ceram Soc 92:2883–2887
18. Hou XR, Zhou SM, Jia TT, Lin H, Teng H (2011) Effect of Nd concentration on structural and optical properties of Nd:Y_2O_3 transparent ceramic. J Lumin 131:1953–1958
19. Wang Y, Lu B, Sun X, Sun T, Xu H (2011) Synthesis of nanocrystalline Sc_2O_3 powder and fabrication of transparent Sc_2O_3 ceramics. Adv Appl Ceram 110:95–98
20. Wang ZJ, Zhou GH, Qin XP, Yang Y, Zhang GJ, Menke Y et al (2014) Transparent $La_{2-x}Gd_xZr_2O_7$ ceramics obtained by combustion method and vacuum sintering. J Alloy Compd 585:497–502
21. Zhou GH, Wang ZJ, Zhou BZ, Zhao Y, Zhang GJ, Wang SW (2013) Fabrication of transparent $Y_2Hf_2O_7$ ceramics via vacuum sintering. Opt Mater 35:774–777
22. Zhou J, Zhang WX, Wang LA, Shen YQ, Li J, Liu WB et al (2011) Fabrication, microstructure and optical properties of polycrystalline Er^{3+}:$Y_3Al_5O_{12}$ ceramics. Ceram Int 37:119–125
23. Zhou J, Zhang WX, Huang TD, Wang LA, Li J, Liu WB et al (2011) Optical properties of Er, Yb co-doped YAG transparent ceramics. Ceram Int 37:513–519
24. Liu WB, Li J, Jiang BX, Zhang D, Pan YB (2012) Effect of La_2O_3 on microstructures and laser properties of Nd:YAG ceramics. J Alloy Compd 512:1–4
25. Li J, Wu YS, Pan YB, Liu WB, Huang LP, Guo JK (2008) Laminar-structured YAG/Nd:YAG/YAG transparent ceramics for solid-state lasers. Int J Appl Ceram Technol 5:360–364
26. Appiagyei KA, Messing GL, Dumm JQ (2008) Aqueous slip casting of transparent yttrium aluminum garnet (YAG) ceramics. Ceram Int 34:1309–1313
27. Li YK, Zhou SM, Lin H, Hou XR, Li WJ, Teng H et al (2010) Fabrication of Nd:YAG transparent ceramics with TEOS, MgO and compound additives as sintering aids. J Alloy Compd 502:225–230
28. Qin XP, Yang H, Zhou GH, Luo DW, Yang Y, Zhang J et al (2012) Fabrication and properties of highly transparent Er:YAG ceramics. Opt Mater 34:973–976
29. Gong H, Tang DY, Huang H, Ma J (2009) Fabrication of yttrium aluminum garnet transparent ceramics from yttria nanopowders synthesized by carbonate precipitation. J Electroceram 23:89–93
30. Qin XP, Zhou GH, Yang H, Wong JI, Zhang J, Luo DW et al (2012) Fabrication and plasma resistance properties of transparent YAG ceramics. Ceram Int 38:2529–2535
31. Gong H, Zhang J, Tang DY, Xie GQ, Huang H, Ma J (2011) Fabrication and laser performance of highly transparent Nd:YAG ceramics from well-dispersed Nd:Y_2O_3 nanopowders by freeze-drying. J Nanopart Res 13:3853–3860
32. Yang H, Qin XP, Zhang J, Ma J, Tang DY, Wang SW et al (2012) The effect of MgO and SiO_2 codoping on the properties of Nd:YAG transparent ceramic. Opt Mater 34:940–943
33. Zhang W, Lu TC, Wei NA, Wang YZ, Ma BY, Li F et al (2012) Assessment of light scattering by pores in Nd:YAG transparent ceramics. J Alloy Compd 520:36–41
34. Ramirez MO, Wisdom J, Li H, Aung YL, Stitt J, Messing GL et al (2008) Three-dimensional grain boundary spectroscopy in transparent high power ceramic laser materials. Opt Express 16:5965–5973
35. Lee SH, Kochawattana S, Messing GL, Dumm JQ, Quarles G, Castillo V (2006) Solid-state reactive sintering of transparent polycrystalline Nd:YAG ceramics. J Am Ceram Soc 89:1945–1950
36. Yagi H, Takaichi K, Ueda K, Yanagitani T, Karninskii AA (2006) Influence of annealing conditions on the optical properties of chromium-doped ceramic $Y_3Al_5O_{12}$. Opt Mater 29:392–396
37. Yagi H, Yanagitani T, Takaichi K, Ueda K, Kaminskii AA (2007) Characterizations and laser performances of highly transparent Nd^{3+}:$Y_3Al_5O_{12}$ laser ceramics. Opt Mater 29:1258–1262

38. Serantoni M, Piancastelli A, Costa AL, Esposito L (2012) Improvements in the production of Yb:YAG transparent ceramic materials: spray drying optimisation. Opt Mater 34:995–1001
39. Chen DJ, Mayo MJ (1996) Rapid rate sintering of nanocrystalline ZrO_2-3mol% Y_2O_3. J Am Ceram Soc 79:906–912
40. Zhang J, Meng F, Todd RI, Fu Z (2010) The nature of grain boundaries in alumina fabricated by fast sintering. Scripta Mater 62:658–661
41. Hou XR, Zhou SM, Li WJ, Li YK (2010) Study on the effect and mechanism of zirconia on the sinterability of yttria transparent ceramic. J Eur Ceram Soc 30:3125–3129
42. Chen PL, Chen IW (1996) Grain boundary mobility in Y_2O_3: defect mechanism and dopant effects. J Am Ceram Soc 79:1801–1809
43. Hamano K, Kanzaki S (1977) Fabrication of transparent spinel ceramics by reactive hot-pressing. J Ceram Soc Jpn 85:225–230
44. Cook R, Kochis M, Reimanis I, Kleebe HJ (2005) A new powder production route for transparent spinel windows: powder synthesis and window properties. In: Tustison RW (ed) Window and dome technologies and materials IX. SPIE-The International Society for Optical Engineering, Bellingham, pp 41–47
45. Zou YT, He DW, Wei XK, Yu RC, Lu TC, Chang XH et al (2010) Nanosintering mechanism of $MgAl_2O_4$ transparent ceramics under high pressure. Mater Chem Phys 123:529–533
46. Lu TC, Chang XH, Qi JQ, Luo XJ, Wei QM, Zhu S, et al (2006) Low-temperature high-pressure preparation of transparent nanocrystalline $MgAl_2O_4$ ceramics. Appl Phys Lett 88 (21):213120–213120
47. Zhang J, Lu TC, Chang XH, Wei N, Xu W (2009) Related mechanism of transparency in $MgAl_2O_4$ nano-ceramics prepared by sintering under high pressure and low temperature. J Phys D-Appl Phys 42(5):052002
48. Chen QY, Meng CM, Lu TC, Chang XH, Ji GF, Zhang L et al (2010) Enhancement of sintering ability of magnesium aluminate spinel ($MgAl_2O_4$) ceramic nanopowders by shock compression. Powder Technol 200:91–95
49. Wollmershauser JA, Feigelson BN, Gorzkowski EP, Ellis CT, Goswami R, Qadri SB et al (2014) An extended hardness limit in bulk nanoceramics. Acta Mater 69:9–16
50. Hall EO (1951) The deformation and aging of mild steel, 3. Discussion of results. Proc Phys Soc Lond Sect B 64:747–753
51. Petch NJ (1953) The cleavage strength of polycrystals. J Iron Steel Inst 174:25–28
52. Liu J, Liu K, Wang HS, Gao F, Liao R (2012) Preparation of silicon nitride porous ceramics. In: Pan W, Gong JH (eds) High-performance ceramics III, parts 1 and 2. Trans Tech Publications Ltd., Stafa-Zurich, pp 824–827
53. Hou XR, Zhou SM, Jia TT, Lin H, Teng H (2011) White light emission in $Tm^{3+}/Er^{3+}/Yb^{3+}$ tri-doped Y_2O_3 transparent ceramic. J Alloy Compd 509:2793–2796
54. Podowitz SR, Gaume R, Feigelson RS (2010) Effect of europium concentration on densification of transparent Eu:Y_2O_3 scintillator ceramics using hot pressing. J Am Ceram Soc 93:82–88
55. Haertling GH, Land CE (1971) Hot-pressed (Pb, La)(Zr, Ti)O_3 ferroelectric ceramics for electrooptic applications. J Am Ceram Soc 54:1–11
56. Jiang H, Zou YK, Chen Q, Li KK, Zhang R, Wang Y et al (2005) Transparent electro-optic ceramics and devices. In: Ming H, Zhang XP, Chen MY (eds) Optoelectronic devices and integration, pts 1 and 2. SPIE-The International Society for Optical Engineering, Bellingham, pp 380–394
57. Sun P, Xu CN, Akiyama M, Watanabe T (1999) Controlled oxygen partial pressure sintering of (Pb, La)(Zr, Ti)O_3 ceramics. J Am Ceram Soc 82:1447–1450
58. Yin QR, Ding AL, Zheng XS, Qiu PS, Shen MR, Cao WW (2004) Preparation and characterization of transparent PZN–PLZT ceramics. J Mater Res 19:729–732
59. Ruan W, Li GR, Zeng JT, Bian JJ, Kamzina LS, Zeng HR et al (2010) Large electro-optic effect in La-doped 0.75Pb($Mg_{1/3}Nb_{2/3}$)O_3-0.25$PbTiO_3$ transparent ceramic by two-stage sintering. J Am Ceram Soc 93:2128–2131

60. Zeng X, He XY, Cheng WX, Qiu PS, Xia B (2014) Effect of Dy substitution on ferroelectric, optical and electro-optic properties of transparent $Pb_{0.90}La_{0.10}(Zr_{0.65}Ti_{0.35})O_3$ ceramics. Ceram Int 40:6197–6202
61. Ji WL, He XY, Cheng WX, Qiu PS, Zeng X, Xia B et al (2015) Effect of La content on dielectric, ferroelectric and electro-optic properties of $Pb(Mg_{1/3}Nb_{2/3})O_3$–$PbTiO_3$ transparent ceramics. Ceram Int 41:1950–1956
62. Giniewicz JR, McHenry DA, Shrout TR, Jang SJ, Bhalla AS, Ainger FW (1990) Characterization of $(1-x)Pb(Mg_{1/3}Nb_{2/3})O_3$-$(x)PbTiO_3$ and $Pb(Sc_{1/2}Ta_{1/2})O_3$ transparent ceramics prepared by uniaxial hot-pressing. Ferroelectrics 109:167–172
63. Su XL, Wang PL, Chen WW, Zhu B, Cheng YB, Yan DS (2004) Translucent α-sialon ceramics by hot pressing. J Am Ceram Soc 87:730–732
64. Xie ZH, Hoffman M, Moon RJ, Munroe PR, Cheng YB (2004) Subsurface indentation damage and mechanical characterization of α-sialon ceramics. J Am Ceram Soc 87:2114–2124
65. Xie ZH, Hoffman M, Cheng YB (2002) Microstructural tailoring and characterization of a calcium alpha-SiAlON composition. J Am Ceram Soc 85:812–818
66. Jones MI, Hyuga H, Hirao K (2003) Optical and mechanical properties of α/β composite sialons. J Am Ceram Soc 86:520–522
67. Fang Y, Agrawal D, Skandan G, Jain M (2004) Fabrication of translucent MgO ceramics using nanopowders. Mater Lett 58:551–554
68. Lyberis A, Stevenson AJ, Suganuma A, Ricaud S, Druon F, Herbst F et al (2012) Effect of Yb^{3+} concentration on optical properties of $Yb:CaF_2$ transparent ceramics. Opt Mater 34:965–968
69. Lyberis A, Patriarche G, Gredin P, Vivien D, Mortier M (2011) Origin of light scattering in ytterbium doped calcium fluoride transparent ceramic for high power lasers. J Eur Ceram Soc 31:1619–1630
70. Swinkels FB, Wilkinson DS, Arzt E, Ashby MF (1983) Mechanism of hot-isostatic pressing. Acta Metall 31:1829–1840
71. Li WB, Ashby MF, Easterling KE (1987) On densification and shape change during hot isostatic pressing. Acta Metall 35:2831–2842
72. Atkinson HV, Davies S (2000) Fundamental aspects of hot isostatic pressing: an overview. Metall Mater Trans A-Phys Metall Mater Sci 31:2981–3000
73. Loh NL, Sia KY (1992) An overview of hot isostatic pressing. J Mater Process Technol 30:45–65
74. Bocanegra-Bernal MH (2004) Hot isostatic pressing (HIP) technology and its applications to metals and ceramics. J Mater Sci 39:6399–6420
75. Petit J, Dethare P, Sergent A, Marino R, Ritti MH, Landais S et al (2011) Sintering of α-alumina for highly transparent ceramic applications. J Eur Ceram Soc 31:1957–1963
76. Krell A, Klimke J (2006) Effects of the homogeneity of particle coordination on solid-state sintering of transparent alumina. J Am Ceram Soc 89:1985–1992
77. Krell A, Klimke J, Hutzler T (2009) Advanced spinel and sub-μm Al_2O_3 for transparent armour applications. J Eur Ceram Soc 29:275–281
78. Krell A, Blank P, Ma HW, Hutzler T, Nebelung M (2003) Processing of high-density submicrometer Al_2O_3 for new applications. J Am Ceram Soc 86:546–553
79. Krell A, Blank P, Ma HW, Hutzler T, van Bruggen MPB, Apetz R (2003) Transparent sintered corundum with high hardness and strength. J Am Ceram Soc 86:12–18
80. Ikesue A, Kamata K (1996) Microstructure and optical properties of hot isostatically pressed Nd:YAC ceramics. J Am Ceram Soc 79:1927–1933
81. Lee SH, Kupp ER, Stevenson AJ, Anderson JM, Messing GL, Li X et al (2009) Hot isostatic pressing of transparent Nd:YAG ceramics. J Am Ceram Soc 92:1456–1463
82. Suarez M, Fernandez A, Menendez JL, Nygren M, Torrecillas R, Zhao Z (2010) Hot isostatic pressing of optically active Nd:YAG powders doped by a colloidal processing route. J Eur Ceram Soc 30:1489–1494

83. Zhang W, Lu TC, Ma BY, Wei N, Lu ZW, Li F et al (2013) Improvement of optical properties of Nd:YAG transparent ceramics by post-annealing and post hot isostatic pressing. Opt Mater 35:2405–2410
84. Dericioglu AF, Kagawa Y (2003) Effect of grain boundary microcracking on the light transmittance of sintered transparent $MgAl_2O_4$. J Eur Ceram Soc 23:951–959
85. Dericioglu AF, Boccaccini AR, Dlouhy I, Kagawa Y (2005) Effect of chemical composition on the optical properties and fracture toughness of transparent magnesium aluminate spinel ceramics. Mater Trans 46:996–1003
86. Esposito L, Piancastelli A, Miceli P, Martelli S (2015) A thermodynamic approach to obtaining transparent spinel ($MgAl_2O_4$) by hot pressing. J Eur Ceram Soc 35:651–661
87. Sutorik AC, Gilde G, Cooper C, Wright J, Hilton C (2012) The effect of varied amounts of LiF sintering aid on the transparency of alumina rich spinel ceramic with the composition $MgO\text{-}1.5Al_2O_3$. J Am Ceram Soc 95:1807–1810
88. Sutorik AC, Gilde G, Swab JJ, Cooper C, Gamble R, Shanholtz E (2012) Transparent solid solution magnesium aluminate spinel polycrystalline ceramic with the alumina-rich composition $MgO\text{-}1.2Al_2O_3$. J Am Ceram Soc 95:636–643
89. Mouzon J, Maitre A, Frisk L, Lehto N, Oden M (2009) Fabrication of transparent yttria by HIP and the glass-encapsulation method. J Eur Ceram Soc 29:311–316
90. Serivalsatit K, Ballato J (2010) Submicrometer grain-sized transparent erbium-doped scandia ceramics. J Am Ceram Soc 93:3657–3662
91. Seeley ZM, Kuntz JD, Cherepy NJ, Payne SA (2011) Transparent Lu_2O_3:Eu ceramics by sinter and HIP optimization. Opt Mater 33:1721–1726
92. Tsukuma K, Yamashita I, Kusunose T (2008) Transparent 8 mol% $Y_2O_3\text{-}ZrO_2$ (8Y) ceramics. J Am Ceram Soc 91:813–818
93. Oh KS, Kim DY, Cho SJ (1995) Shrinkage of large isolated pores during hot isostatic pressing of presintered alumina ceramics. J Am Ceram Soc 78:2537–2540
94. Sakuma T, Ikuhara Y, Takigawa Y, Thavorniti P (1997) Importance of grain boundary chemistry on the high-temperature plastic flow in oxide ceramics. Mater Sci Eng A-Struct Mater Prop Microstruct Process 234:226–229
95. Yoshida H, Kuwabara A, Yamamoto T, Ikuhara Y, Sakuma T (2005) High temperature plastic flow and grain boundary chemistry in oxide ceramics. J Mater Sci 40:3129–3135
96. Hayashi K, Kobayashi O, Toyoda S, Morinaga K (1991) Transmission optical-properties of polycrystalline alumina with submicro grains. Mater Trans JIM 32:1024–1029
97. Tsukuma K (2006) Transparent $MgAl_2O_4$ spinel ceramics produced by HIP post-sintering. J Ceram Soc Jpn 114:802–806
98. Cherepy NJ, Kuntz JD, Roberts JJ, Hurst TA, Drury OB, Sanner RD et al (2008) Transparent ceramic scintillator fabrication, properties and applications. In: Burger A, Franks LA, James RB (eds) Hard X-ray, gamma-ray, and neutron detector physics X. SPIE-The International Society for Optical Engineering, Bellingham
99. Alberta EF, Bhalla AS (2001) Piezoelectric and dielectric properties of transparent $Pb(Ni_{1/3}Nb_{2/3})_{1\text{-}x\text{-}y}Zr_xTi_yO_3$ ceramics prepared by hot isostatic pressing. Int J Inorg Mater 3:987–995
100. Schneider H, Schmucker M, Ikeda K, Kaysser WA (1993) Optically translucent mullite ceramics. J Am Ceram Soc 76:2912–2914
101. Aubry P, Bensalah A, Gredin P, Patriarche G, Vivien D, Mortier M (2009) Synthesis and optical characterizations of Yb-doped CaF_2 ceramics. Opt Mater 31:750–753
102. Uematsu K, Takagi M, Honda T, Uchida N, Saito K (1989) Transparent hydroxyapatite prepared by hog isostatic pressing of filter cake. J Am Ceram Soc 72:1476–1478
103. Mandal H (1999) New developments in α-SiAlON ceramics. J Eur Ceram Soc 19:2349–2357
104. Itatani K, Tsujimoto T, Kishimoto A (2006) Thermal and optical properties of transparent magnesium oxide ceramics fabricated by post hot-isostatic pressing. J Eur Ceram Soc 26:639–645
105. Ji YM, Jiang DY, Fen T, Shi JL (2005) Fabrication of transparent $La_2Hf_2O_7$ ceramics from combustion synthesized powders. Mater Res Bull 40:553–559

106. Roussel N, Lallemant L, Durand B, Guillemet S, Ching JYC, Fantozzi G et al (2011) Effects of the nature of the doping salt and of the thermal pre-treatment and sintering temperature on spark plasma sintering of transparent alumina. Ceram Int 37:3565–3573
107. Kim BN, Hiraga K, Morita K, Yoshida H (2007) Spark plasma sintering of transparent alumina. Scripta Mater 57:607–610
108. Wang C, Zhao Z (2010) Transparent polycrystalline ruby ceramic by spark plasma sintering. Mater Res Bull 45:1127–1131
109. Jin XH, Gao L, Sun J (2010) Highly transparent alumina spark plasma sintered from common-grade commercial powder: the effect of powder treatment. J Am Ceram Soc 93:1232–1236
110. Aman Y, Garnier V, Djurado E (2009) Influence of green state processes on the sintering behaviour and the subsequent optical properties of spark plasma sintered alumina. J Eur Ceram Soc 29:3363–3370
111. Dang KQ, Takei S, Kawahara M, Nanko M (2011) Pulsed electric current sintering of transparent Cr-doped Al_2O_3. Ceram Int 37:957–963
112. Nanko M, Dang KQ (2014) Two-step pulsed electric current sintering of transparent Al_2O_3 ceramics. Adv Appl Ceram 113:80–84
113. Chaim R, Marder-Jaeckel R, Shen JZ (2006) Transparent YAG ceramics by surface softening of nanoparticles in spark plasma sintering. Mater Sci Eng A-Struct Mater Prop Microstruct Process 429:74–78
114. Chaim R, Kalina M, Shen JZ (2007) Transparent yttrium aluminum garnet (YAG) ceramics by spark plasma sintering. J Eur Ceram Soc 27:3331–3337
115. An LQ, Ito A, Goto T (2011) Two-step pressure sintering of transparent lutetium oxide by spark plasma sintering. J Eur Ceram Soc 31:1597–1602
116. Yoshida H, Morita K, Kim BN, Hiraga K, Yamanaka K, Soga K et al (2011) Low-temperature spark plasma sintering of yttria ceramics with ultrafine grain size. J Am Ceram Soc 94:3301–3307
117. Yoshida H, Morita K, Kim BN, Hiraga K, Kodo M, Soga K et al (2008) Densification of nanocrystalline yttria by low temperature spark plasma sintering. J Am Ceram Soc 91:1707–1710
118. Zhang HB, Kim BN, Morita K, Yoshida H, Hiraga K, Sakka Y (2011) Fabrication of transparent yttria by high-pressure spark plasma sintering. J Am Ceram Soc 94:3206–3210
119. An LQ, Ito A, Goto T (2012) Transparent yttria produced by spark plasma sintering at moderate temperature and pressure profiles. J Eur Ceram Soc 32:1035–1040
120. An LQ, Ito A, Goto T (2011) Fabrication of transparent lutetium oxide by spark plasma sintering. J Am Ceram Soc 94:695–698
121. Anselmi-Tamburini U, Woolman JN, Munir ZA (2007) Transparent nanometric cubic and tetragonal zirconia obtained by high-pressure pulsed electric current sintering. Adv Funct Mater 17:3267–3273
122. Zhang HB, Kim BN, Morita K, Hiraga HYK, Sakka Y (2011) Effect of sintering temperature on optical properties and microstructure of translucent zirconia prepared by high-pressure spark plasma sintering. Sci Technol Adv Mater 12:055003
123. Lei LW, Fu ZY, Wang H, Lee SW, Niihara K (2012) Transparent yttria stabilized zirconia from glycine-nitrate process by spark plasma sintering. Ceram Int 38:23–28
124. Chaim R, Shen ZJ, Nygren M (2004) Transparent nanocrystalline MgO by rapid and low-temperature spark plasma sintering. J Mater Res 19:2527–2531
125. Frage N, Cohen S, Meir S, Kalabukhov S, Dariel MP (2007) Spark plasma sintering (SPS) of transparent magnesium-aluminate spinel. J Mater Sci 42:3273–3275
126. Meir S, Kalabukhov S, Froumin N, Dariel MP, Frage N (2009) Synthesis and densification of transparent magnesium aluminate spinel by SPS processing. J Am Ceram Soc 92:358–364
127. Morita K, Kim BN, Hiraga K, Yoshida H (2008) Fabrication of transparent $MgAl_2O_4$ spinel polycrystal by spark plasma sintering processing. Scripta Mater 58:1114–1117

128. Zhang GM, Wang YC, Fu ZY, Wang H, Wang WM, Zhang JY et al (2009) Transparent mullite ceramic from single-phase gel by spark plasma sintering. J Eur Ceram Soc 29:2705–2711
129. Zhang GM, Fu ZY, Wang YC, Wang H, Wang WM, Zhang JY (2009) Effect of precursors on transmittance and microstructure of mullite ceramics. In: Kim H, Yang JF, Sekino T, Lee SW (eds) Eco-materials processing and design X. p 429–432
130. Watanabe Y, Ikoma T, Monkawa A, Suetsugu Y, Yamada H, Tanaka J et al (2005) Fabrication of transparent hydroxyapatite sintered body with high crystal orientation by pulse electric current sintering. J Am Ceram Soc 88:243–245
131. Eriksson M, Liu Y, Hu JF, Gao L, Nygren M, Shen ZJ (2011) Transparent hydroxyapatite ceramics with nanograin structure prepared by high pressure spark plasma sintering at the minimized sintering temperature. J Eur Ceram Soc 31:1533–1540
132. An L, Ito A, Goto T (2011) Fabrication of transparent Lu_3NbO_7 by spark plasma sintering. Mater Lett 65:3167–3169
133. Xiong Y, Fu ZY, Wang YC, Quan F (2006) Fabrication of transparent AIN ceramics. J Mater Sci 41:2537–2539
134. Wu YJ, Kimura R, Uekawa N, Kakegawa K, Sasaki Y (2002) Spark plasma sintering of transparent $PbZrO_3$–$PbTiO_3$–$Pb(Zn_{1/3}Nb_{2/3})O_3$ ceramics. Japan J Appl Phys Part 2-Lett 41: L219–L221
135. Wu YJ, Li J, Kimura R, Uekawa N, Kakegawa K (2005) Effects of preparation conditions on the structural and optical properties of spark plasma-sintered PLZT (8/65/35) ceramics. J Am Ceram Soc 88:3327–3331
136. Liu J, Shen ZJ, Yao WL, Zhao YH, Mukherjee AK (2010) Visible and infrared transparency in lead-free bulk $BaTiO_3$ and $SrTiO_3$ nanoceramics. Nanotechnology 21:075706
137. Wu YJ, Wang N, Wu SY, Chen XM (2011) Transparent barium strontium titanate ceramics prepared by spark plasma sintering. J Am Ceram Soc 94:1343–1345
138. Kim B-N, Hiraga K, Morita K, Yoshida H (2009) Effects of heating rate on microstructure and transparency of spark-plasma-sintered alumina. J Eur Ceram Soc 29:323–327
139. Jiang D, Hulbert DM, Anselmi-Tamburini U, Ng T, Land D, Mukherjee AK (2007) Spark plasma sintering and forming of transparent polycrystalline Al_2O_3 windows and domes. In: Tustison RW (ed) Window and dome technologies and materials X. SPIE-The International Society for Optical Engineering, Bellingham, p 54509
140. Wang C, Zhao Z (2009) Transparent $MgAl_2O_4$ ceramic produced by spark plasma sintering. Scripta Mater 61:193–196
141. Krell A, Blank P (1995) Grain-size dependence of hardness in dense submicrometer alumina. J Am Ceram Soc 78:1118–1120
142. Palmero P, Bonelli B, Fantozzi G, Spina G, Bonnefont G, Montanaro L et al (2013) Surface and mechanical properties of transparent polycrystalline YAG fabricated by SPS. Mater Res Bull 48:2589–2597
143. An LQ, Ito A, Goto T (2011) Highly transparent lutetium titanium oxide produced by spark plasma sintenng. J Eur Ceram Soc 31:237–240
144. An LQ, Ito A, Goto T (2012) Effect of calcination temperature on the fabrication of transparent lutetium titanate by spark plasma sintering. Ceram Int 38:4973–4977
145. An LQ, Ito A, Goto T (2013) Fabrication of transparent $Lu_2Hf_2O_7$ by reactive spark plasma sintering. Opt Mater 35:817–819
146. An LQ, Ito A, Goto T (2011) Fabrication of transparent Lu_3NbO_7 by spark plasma sintering. Mater Lett 65:3167–3169
147. An LQ, Ito A, Goto T (2013) Transparent Lu_3NbO_7 bodies prepared by reactive spark plasma sintering and their optical and mechanical properties. Ceram Int 39:383–387
148. Sahin FC, Kanbur HE, Apak B (2012) Preparation of AlON ceramics via reactive spark plasma sintering. J Eur Ceram Soc 32:925–929
149. Chen S, Wu YQ, Yang Y (2013) Spark plasma sintering of hexagonal structure Yb^{3+}-doped $Sr_5(PO_4)_3F$ transparent ceramics. J Am Ceram Soc 96:1694–1697

150. Cheng JP, Agrawal D, Zhang YJ, Roy R (2002) Microwave sintering of transparent alumina. Mater Lett 56:587–592
151. Brosnan KH, Messing GL, Agrawal DK (2003) Microwave sintering of alumina at 2.45 GHz. J Am Ceram Soc 86:1307–1312
152. Fang Y, Cheng JP, Agrawal DK (2004) Effect of powder reactivity on microwave sintering of alumina. Mater Lett 58:498–501
153. Esposito L, Piancastelli A, Bykov Y, Egorov S, Eremeev A (2013) Microwave sintering of Yb:YAG transparent laser ceramics. Opt Mater 35:761–765
154. Cheng JP, Agrawal D, Zhang YJ, Roy R (2001) Microwave reactive sintering to fully transparent aluminum oxynitride (AlON) ceramics. J Materi Sci Lett 20:77–79
155. Fang Y, Roy R, Agrawal DK, Roy DM (1996) Transparent mullite ceramics from diphasic aerogels by microwave and conventional processings. Mater Lett 28:11–15
156. Li MJ, Wu YC, Yen FS, Huang CY (2011) Influence of ionic mobility on the phase transformation route in $Y_3Al_5O_{12}$ (YAG) stoichiometry. J Eur Ceram Soc 31:2099–2106
157. Rybakov KI, Semenov VE (1994) Possibility of plastic-deformation of an ionic-crystal due to the nonthermal influence of a high-frequency electric-field. Phys Rev B 49:64–68
158. Rybakov KI, Semenov VE (1995) Mass-transport in ionic-crystals induced by the ponderomotive action of a high-frequency electric-field. Phys Rev B 52:3030–3033